





Infrared galaxies detected by the Atacama Cosmology Telescope

ECE KILERCI ¹, TETSUYA HASHIMOTO ², TOMOTSUGU GOTO ³, ERSIN GÖĞÜŞ ¹, SEONG JIN KIM ³,
SIMON C.-C. HO ⁴, AND YI HANG VALERIE WONG ⁵

¹*Sabancı University, Faculty of Engineering and Natural Sciences, 34956, Istanbul, Turkey*

²*Department of Physics, National Chung Hsing University, No. 145, Xingda Rd., South Dist., Taichung, 40227, Taiwan (R.O.C.)*

³*Institute of Astronomy, National Tsing Hua University, 101, Section 2, Kuang-Fu Road, Hsinchu, 30013, Taiwan (R.O.C.)*

⁴*Research School of Astronomy and Astrophysics, The Australian National University, Canberra, ACT 2611, Australia*

⁵*Department of Astrophysical and Planetary Sciences, University of Colorado Boulder, CO 80309, USA*

ABSTRACT

We report on 167 infrared (IR) galaxies selected by AKARI and IRAS and detected in the Atacama Cosmology Telescope (ACT) Data Release 5 (DR5) sky maps at the 98, 150 and 220 GHz frequency bands. Of these detections, 134 (80%) of the millimeter counterparts are first-time identifications with ACT. We expand the previous ACT extragalactic source catalogs, by including new 98 GHz detections and measurements from ACT DR5. We also report flux density measurements at the 98, 150, and 220 GHz frequency bands. We compute α_{98-150} , α_{98-220} , and $\alpha_{150-220}$ millimeter-wave spectral indices and far-IR to millimeter-wave spectral indices between 90 μm and 98, 150, and 220 GHz. We specify the galaxy type, based on $\alpha_{150-220}$. We combine publicly available multiwavelength data-including ultraviolet, optical, near-IR, mid-IR, far-IR, and the millimeter measurements obtained in this work-and perform spectral energy distribution (SED) fitting with CIGALE. With the radio emission decomposition advantage of CIGALE V2022.0, we identify the origins of the millimeter emissions for 69 galaxies in our sample. Our analysis also shows that millimeter data alone indicates the need for a radio synchrotron component in the SEDs that are produced by active galactic nuclei (AGNs) and/or star formation. We present SEDs and measured physical properties of these galaxies, such as the dust luminosity, AGN luminosity, the total IR luminosity, and the ratio of the IR and radio luminosity. We quantify the relationships between the total IR luminosity and the millimeter-band luminosities, which can be used in the absence of SED analysis.

Keywords: galaxies: active –infrared: galaxies – radio continuum: galaxies

1. INTRODUCTION

Infrared (IR) galaxies (e.g., Sanders & Mirabel 1996; Lonsdale et al. 2006) emit most of their radiation at mid-IR to far-IR (FIR) wavelengths, due to their dust content. Dust absorbs the optical and ultraviolet (UV) radiation produced by star formation (SF) and active galactic nuclei (AGNs), then re-emits it in the IR, sub-millimeter, and millimeter wavelengths. IR galaxies are classified according to their total IR luminosity (L_{IR} , integrated over $-3-1000 \mu\text{m}$) as luminous IR galaxies (LIRGs; $10^{11} L_{\odot} < L_{\text{IR}} < 10^{12} L_{\odot}$) and ultraluminous

IR galaxies (ULIRGs; $10^{12} L_{\odot} < L_{\text{IR}} < 10^{13} L_{\odot}$). It is noteworthy that LIRGs and ULIRGs, which are relatively rare in the local universe (e.g., Le Floc’h et al. 2005; Goto et al. 2010; Rodighiero et al. 2010; Kilerci Eser & Goto 2018), are major systems of SF at the peak ($z \sim 1-2$) of cosmic SF activity (e.g., Rowan-Robinson 2001; Goto et al. 2010). Therefore, it is highly important to have a complete understanding of IR galaxies and the evolution of their SF. The main processes controlling the evolutions of galaxies are SF and AGN activity (i.e. black hole accretion). After their peak, between $z \sim 1-3$, these two phenomena declined toward the present epoch. At the present epoch, however, the dusty star-forming IR galaxies do not follow this decline, representing the higher-redshift population of IR galaxies. For normal galaxies at the present epoch es-

pecially, AGN feedback is expected to reduce the star formation rate (SFR). On the other hand, both processes are working simultaneously in the IR galaxies at this epoch. These separate processes can be quantified by accurate measurements of the physical parameters of galaxies, such as the stellar mass, SFR, dust mass, and the AGN contribution to the total luminosity. All of these parameters can be directly obtained from spectral energy distributions (SEDs).

The first attempts to model the SEDs of IR galaxies only included the parameterization of the IR luminosity (e.g., Sanders & Mirabel 1996; Chary & Elbaz 2001; Rieke et al. 2009). In addition, models obtained from observed galaxy SEDs with one or two parameters have been widely used for IR SEDs (e.g., Dale & Helou 2002; Dale et al. 2014). Recently, we have attained a better understanding of the physical properties of IR galaxies, by using more sophisticated SED tools, such as the Code for Investigating Galaxy Emission (CIGALE; Noll et al. 2009; Serra et al. 2011; Boquien et al. 2019), which requires the energy balance between the absorbed UV-to-optical emission and the re-emitted IR emission, with the presence of AGNs as well. Due to the limited wavelength coverage of current space telescopes—such as AKARI (Murakami et al. 2007), the Spitzer Space Telescope (Werner et al. 2004), and the Herschel Space Observatory (Herschel; Pilbratt et al. 2010)—the longest FIR wavelength to be included in SEDs is $\sim 600\mu\text{m}$. Beyond the FIR region, the IR—radio correlation (Helou et al. 1985) between the L_{IR} and the radio luminosity at 1.4 GHz is well known for radio galaxies, and can be used to trace SF (e.g., Murphy et al. 2011, 2012). On the other hand, the millimeter region of the SED—that is, between the peak of the SED and the radio region—is not a deeply explored domain. In particular, the information that could be gained from the millimeter data has not been carefully examined for SEDs of IR galaxies. The millimeter data have the potential to constrain the SED beyond the peak ($\sim 90\text{--}100\mu\text{m}$), especially in the absence of FIR measurements. Additionally, the millimeter bands also provide an effective tool for selecting higher-redshift dusty star-forming galaxies (DSFGs; see, e.g., Casey et al. 2021; Zavala et al. 2021), due to the negative K -correction (especially in the 2 mm band), and for measuring the contributions of DSFGs to the cosmic SF beyond redshift $z = 3$. The scope of this work is to systematically explore the millimeter regions in the SEDs of a large sample of IR galaxies, to better describe the SEDs up to radio, to investigate the origin of the millimeter emission, and to obtain better insights into the physical properties of IR galaxies, such as their

stellar masses, dust masses, SFRs and AGN contributions to the total IR luminosity.

The main purpose of millimeter-wave surveys is to measure primordial fluctuations in the cosmic microwave background (CMB; e.g.; Das et al. 2011; Story et al. 2013; Planck Collaboration et al. 2014a,b, 2020). Foreground extragalactic sources also emit at millimeter wavelengths, between 90 and 220 GHz (1.3–3.0 mm). These sources are mainly AGNs, DSFGs, gravitationally lensed DSFGs, and galaxy clusters. AGN accretion disks produce jets composed of ionized relativistic matter traveling around magnetic field lines. When the direction of such a jet is toward us, the system is called a blazar (Urry & Padovani 1995). The blazar jets generate synchrotron emission (Ulrich et al. 1997). DSFGs are also referred as IR galaxies, due to the significant IR radiation that is produced by the dust that is heated by the radiation of the SF and/or the AGN continuum radiation. This thermal dust emission extends to the millimeter wavelength region. AGNs at the centers of such galaxies also have contributions to the millimeter-wave emission as nonthermal radiation. Galaxy clusters can be mapped due to the thermal Sunyaev–Zel’dovich effect (e.g., Sunyaev & Zeldovich 1972), as a distortion of the CMB spectrum at millimeter wavelengths (e.g., Hilton et al. 2021).

Due to the technical capacities of telescopes, such as the large beam sizes and the limited small sky surveys (mostly up to 10 deg^2), the study of the millimeter-wave properties of extragalactic sources has recently become a developing area (e.g., Vieira et al. 2010; Marriage et al. 2011; Mocanu et al. 2013; Marsden et al. 2014; Planck Collaboration et al. 2014a; Gralla et al. 2020; Everett et al. 2020; Reuter et al. 2020). The Planck space telescope (Planck Collaboration et al. 2011) has observed the entire sky in the 30–875 GHz (9993–343 μm), frequency regime and cataloged several extragalactic sources (Planck Collaboration and Aalto et al. 2011; Planck Collaboration et al. 2016; Lianou et al. 2019). With its large beam size of $\sim 5' - 7'$, Planck can detect bright sources above $\gtrsim 400\text{ mJy}$ at 143 and 217 GHz (Planck Collaboration et al. 2016). Additionally, the South Pole Telescope (SPT; Vieira et al. 2010; Carlstrom et al. 2011), which is a 10 m millimeter telescope with arcminute resolution that is located at the National Science Foundation Amundsen–Scott South Pole Station in Antarctica, has scanned the southern hemisphere. The SPT had three millimeter bands, at 95, 150, and 220 GHz with 9.8, 5.8, and 20.5 mJy detection limits, respectively (Everett et al. 2020). A large sample of millimeter-wave extragalactic sources (more than 4000) have been iden-

tified and cataloged (Vieira et al. 2010; Mocanu et al. 2013; Everett et al. 2020; Reuter et al. 2020) in the SPT Sunyaev–Zel’dovich survey (Vieira et al. 2010), which was completed between 2008 and 2011, over an area of ~ 2530 square degrees.

The Atacama Cosmology Telescope (ACT; Swetz et al. 2011; Thornton et al. 2016) is a 6 meter ground-based telescope that is designed to survey the CMB. ACT started observing in 2007, with its first-generation Millimeter Bolometric Array Camera (Fowler et al. 2007; Swetz et al. 2011), then between 2013 and 2015 it used ACTPol camera (Thornton et al. 2016), which improved the sensitivity of polarization measurements. Since 2016, ACT has been observing with the Advanced ACT-Pol camera (Henderson et al. 2016), which has mapped almost half of the sky in five frequency bands, at 30, 40, 98, 150, and 220 GHz, at an angular resolution of a few arcminutes, with increased sensitivity. Recently, the latest ACT Data Release 5 (DR5; Naess et al. 2020) included merged maps at 90, 150, and 220 GHz obtained between the 2008 and 2018 observing seasons. Note that the Planck measurements at 143 and 217 GHz are analogous to those at the 150 and 220 GHz frequencies of ACT. However, with a finer angular resolution ($\sim 1.5'$) and a lower detection threshold (~ 20 mJy at 150 GHz; Datta et al. 2019), ACT has a great advantage in detecting sources with lower brightness.

The first catalog of extragalactic millimeter sources detected by ACT was presented by Marriage et al. (2011). Their report 157 extragalactic sources, including clusters and radio sources, which were detected at 148 GHz during the 2008 observations. Marriage et al. (2011) noted that most of these sources were detected at lower radio frequencies. They also determined the dominant radiation processes and spectral indices for these systems by cross-identifications with other catalogs, including the NASA/IPAC Extragalactic Database (NED), the REFLEX cluster catalog (Böhringer et al. 2004), the Infrared Astronomical Satellite (IRAS) Point Source Catalog (Helou & Walker 1988), the Sydney University Molonglo Sky Survey (SUMSS) 0.84 GHz catalog (Mauch et al. 2003), the SPT 2.0 mm catalog (Vieira et al. 2010), and the Australia Telescope 20 GHz (AT20G) 5, 8, and 20 GHz catalogs (Murphy et al. 2010). Additionally, they examined the color-color comparisons at 5–20 GHz and 20–148 GHz for 109 ACT–AT20G sources, finding median spectral indices of $\alpha_{5-20} = -0.07 \pm 0.37$ and $\alpha_{20-148} = -0.39 \pm 0.24$, indicating spectral steepening between these frequencies (Marriage et al. 2011).

Marsden et al. (2014) presented an extended catalog, containing 191 extragalactic sources detected by ACT

from 148 and 218 GHz maps that were obtained between 2007 and 2010. Their sample included 167 radio galaxies that were powered by AGNs and 24 DSFGs. Marsden et al. (2014) identified counterparts of their sample at 0.84 GHz (from SUMSS; Mauch et al. 2003), 4.86 GHz (from the Parkes-MIT-NRAO survey; Wright et al. 1994), and 20 GHz (from the AT20G survey; Murphy et al. 2010), as well as in the 1.4/2.0 mm (from the SPT survey; Vieira et al. 2010) and 12–100 μm bands (from IRAS; Helou & Walker 1988). Marsden et al. (2014) included 20 GHz measurements from follow-up ATCA observations for 41 sources, reporting a steepening slope of the SED from 20 to 218 GHz for synchrotron-dominated galaxies. The nature of the millimeter sources could be identified from the spectral index, α , of the power-law spectra $S_\nu \sim \nu^\alpha$ (Marsden et al. 2014). The dust-dominated galaxies in their sample exhibited a median spectral index of $\alpha_{148-218} = 3.7^{+0.62}_{-0.86}$. They reported a spectral index of $\alpha_{148-218} = -0.6$ for synchrotron-dominated sources (Marsden et al. 2014).

Datta et al. (2019) presented three extragalactic point-source catalogs derived from ACT Data Release 3 (DR3), covering three sky regions. The ACT DR3 observations were obtained with ACTPol between 2013 and 2014. The ACT DR3 point-source catalogs that mostly included synchrotron-dominated blazars provided flux densities at 150 GHz and polarization properties. Based on the crossmatched counterpart flux densities from the National Radio Astronomy Observatory Very Large Array Sky Survey (Condon et al. 1998) and the Very Large Array–Faint Images of the Radio Sky at Twenty-Centimeters (VLA-FIRST; Becker et al. 1995), AT20G, ACT Equatorial, and Herschel Spectral and Photometric Receiver (SPIRE) surveys, they derived mean spectral indices of $\alpha_{20-148} = -0.36$, $\alpha_{1.4-148} = -0.21$. Datta et al. (2019) listed 19 potential DSFG candidates based on their spectral indices. Recently, Gralla et al. (2020) have prepared a catalog of ACT Equatorial survey extragalactic sources, including 510 AGNs and 287 DSFGs. Their catalog reports the flux density measurements at the 148 GHz, 218 GHz, and 277 GHz frequency bands. They also present the spectral properties of DSFGs, including both lensed sources and nearby unlensed sources (Gralla et al. 2020).

FIR counterparts observed with IRAS, AKARI, Herschel, and Spitzer of some of the local DSFGs identified at ACT wavelengths have been reported by Marsden et al. (2014) and Gralla et al. (2020). The catalog of Marsden et al. (2014) has a few nearby IRAS galaxies, with synchrotron- or dust-dominated spectra. AKARI completed the most recent all-sky survey in the mid-IR and FIR, detecting thousands of IR galaxies in the low-

redshift ($z \leq 0.3$) universe (Kilerci Eser & Goto 2018). Therefore, we base our investigation on the AKARI-detected galaxies and select IR galaxies that overlap with the area mapped by the ACT. We identify and select IR galaxies that have been detected by IRAS or AKARI in the publicly released ACT DR5 sky maps at 98, 150, and 220 GHz. Throughout the paper, we refer to the ACT frequency band centered at 224 GHz as 220 GHz band. In order to avoid DSFGs that have possibly been lensed by foreground galaxies, we restrict our investigation to spectroscopically confirmed low-redshift ($z < 0.35$) IR galaxies with IRAS–AKARI detections at FIR bands.

Our goal is to investigate the origins of the measured millimeter emission from the SEDs and to measure physical properties of the local DSFGs that have been detected by ACT. In order to investigate the origins of the millimeter emission, for the first time, we take advantage of the latest version of CIGALE, which can decompose the radio emissions from SF and AGNs separately. We also aim to examine the relationships between the total IR luminosity and the millimeter-band luminosities that have not been reported for low-redshift ($z < 0.35$) IR galaxies with millimeter counterparts.

The structure of this paper is organized as follows. In §2, we present the IRAS–AKARI–ACT sample selection, the ACT source detection, and the multiwavelength data of our ACT-detected IRAS–AKARI IR galaxy sample. In §3, we present our analysis of the spectral indices and the SEDs. In §4, we discuss our results. Our conclusions are summarized in §5. Throughout this paper, we adopt a flat Λ cold dark matter cosmology, with $H_0 = 72 \text{ km s}^{-1} \text{ Mpc}^{-1}$, $\Omega_\Lambda = 0.7$, and $\Omega_m = 0.3$ (Spergel et al. 2003).

2. SAMPLE SELECTION AND DATA

2.1. IRAS–AKARI–ACT Sample Selection

The goal of this work is to study the UV-to-millimeter wave emission properties of IR galaxies that have been detected with IRAS or AKARI and ACT. IRAS and AKARI satellite are the two major telescopes that have scanned the whole sky and observed IR galaxies. IRAS scanned all the sky in four IR bands, centered at $12 \mu\text{m}$, $25 \mu\text{m}$, $60 \mu\text{m}$, and $100 \mu\text{m}$. The IRAS Point Source Catalog Redshift (PSCz) survey (Saunders et al. 2000) includes 15,411 IRAS galaxies with secure spectroscopic redshifts. Among those, 4954 galaxies are within the ACT DR5 sky region.

The AKARI satellite (Murakami et al. 2007) conducted mid-IR and FIR all-sky surveys at 9 and $18 \mu\text{m}$ and at 65, 90, 140, and $160 \mu\text{m}$, respectively. The AKARI/FIS all-sky survey bright source catalog version

2¹ (Yamamura et al. 2018) (Yamamura et al. 2018) includes FIR flux measurements of 918,056 IR sources. These sources are detected due to their dust emissions, with the SEDs peaking around $100 \mu\text{m}$. From these, we select 166,625 IR sources within the ACT DR5 sky coverage ($-180^\circ < \text{RA} < 180^\circ$ and $-63^\circ < \text{decl.} < 23^\circ$). In order to identify the galaxies among these IR sources, we crossmatch with the optical counterparts within $20''$ from the Sloan Digital Sky Survey (SDSS) Data Release 17 (DR17; Abdurro'uf et al. 2022), the Six-degree Field Galaxy Survey (6dFGS; Jones et al. 2004, 2005, 2009), the Two Micron All Sky Survey (2MASS; Huchra et al. 2005, 2012), and the IRAS PSCz (Saunders et al. 2000) spectroscopic redshift catalogs. As a result, we identify 12,559 spectroscopically confirmed IR galaxies as detected by AKARI that overlap with the ACT DR5 sky coverage. 1145 of these 12,559 galaxies are among the 4954 IRAS galaxies. The IRAS galaxy sample includes 3809 galaxies that are not in the AKARI galaxy sample. The AKARI sample has 11,414 galaxies that are not in the IRAS galaxy sample. Therefore, our initial IRAS–AKARI infrared galaxy sample includes 16,368 galaxies.

2.2. ACT Source Detection

In the following, we explain the ACT source detection procedure in two steps: (i) the applied empirical flux calibration; and (ii) the source detection with Source-Extractor.

2.2.1. Empirical Flux Calibration

The latest ACT DR5 includes the deepest data obtained between 2008 and 2018 (Naess et al. 2020). We use the coadded 98 GHz, 150 GHz, and 220 GHz day–night maps, combined with Planck data. The point-source FWHMs (FWHM_{PSF}) of the coadded maps are $2.1'$, $1.3'$, and $1.0'$ at 98 GHz, 150 GHz, and 220 GHz, respectively. These FWHM_{PSF} are larger than the individual galaxy sizes, except for very nearby sources. Therefore, individual galaxies are expected to appear as point sources in most cases. However, the DR5 point-source catalog has not yet been released, as of 2022 November. The available point-source catalog is for DR3 at 150 GHz (Datta et al. 2019). Therefore, we use the DR3 map and its point-source catalog to empirically calibrate our source detection in DR5, as described in the following paragraphs.

We subtract background radiation from the DR3 map using Source-Extractor V2.19.5 (Bertin & Arnouts

¹ <http://www.ir.isas.jaxa.jp/AKARI/Archive/Catalogues/FISBSCv2/>

1996). The adopted background mesh size is 4 pixels, which is larger than the DR3 FWHM size of 2.8 pixels. The GLOBAL background type is selected in this procedure. Aperture photometry is performed for the background-subtracted DR3 map, with a $1.0 \times \text{FWHM}_{\text{PSF}}$ diameter. In Fig. 1, $\log(T_{\text{ap,DR3}}/T_{\text{cat,DR3}})$ as a function of $\log T_{\text{cat,DR3}}$ in units of μK are shown for sources in the DR3 point-source catalog (Datta et al. 2019). Here, $T_{\text{ap,DR3}}$ and $T_{\text{cat,DR3}}$ are the DR3 differential CMB temperature measured within the aperture and the differential CMB temperature in the DR3 point-source catalog, respectively. The observed frequency is 150 GHz. If $T_{\text{ap,DR3}} = T_{\text{cat,DR3}}$, the data should be distributed around $y = 0$ (dashed black line). The slope of the best-fit linear function to the data (solid blue line) is ~ 0 , whereas $\log(T_{\text{ap,DR3}}/T_{\text{cat,DR3}})$ shows a systematic offset of -0.379 dex from $y = 0$. This systematic offset is due to the aperture effect, which misses the flux density at the outer part of the point spread function (PSF). We use this -0.379 dex for the aperture correction in the following analyses.

The aperture photometry for the DR5 map at 150 GHz is conducted by following the same procedure as for the DR3 map. The DR5 map is provided in units of μK . The measured DR5 differential CMB temperatures are corrected for aperture effect and are empirically converted from μK to mJy ($f_{\text{apcor,DR5}}$), using the median value of the conversion factors in the DR3 point-source catalog. In Fig. 2, $\log(f_{\text{apcor,DR5}}/f_{\text{cat,DR3}})$ as a function of $\log f_{\text{cat,DR3}}$ in units of mJy are shown for sources in the DR3 point-source catalog. $f_{\text{cat,DR3}}$ is the flux density in the DR3 point-source catalog. The slope and intercept of the best-fit linear function to the data points (solid blue line) are both ~ 0 , indicating that the systematic uncertainty of our flux calibration is negligible. However, the data dispersion around the best-fit linear function is $\sigma_{\log f} = 0.096$, which corresponds to a $\sim 20\%$ statistical uncertainty of the flux density in linear scale. Therefore, the measured flux densities in this work include uncertainties arising from this flux calibration and from background noises. We take both into account in the SED fitting analysis described in §3.

The flux calibration mentioned above is for ACT maps at 150 GHz. The FWHM_{PSF} of DR5 maps at 98 and 220 GHz are different from that at 150 GHz. Therefore, the conversion factors between μK and mJy are also different at 98 and 220 GHz. Following the literature (e.g., Planck Collaboration et al. 2014a)², we scale the

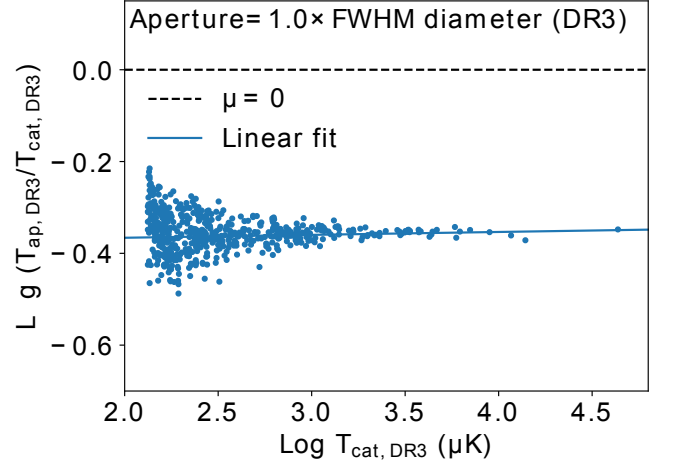


Figure 1. $\log(T_{\text{ap,DR3}}/T_{\text{cat,DR3}})$ as a function of $\log T_{\text{cat,DR3}}$ for sources in the DR3 point-source catalog (Datta et al. 2019). Here, $T_{\text{ap,DR3}}$ is the DR3 differential CMB temperature measured within an aperture with a $1.0 \times \text{FWHM}_{\text{PSF}}$ diameter. $T_{\text{cat,DR3}}$ is the differential CMB temperature in the DR3 point-source catalog. The observed frequency is 150 GHz. The horizontal dashed black line indicates $y = 0$, while the solid blue line is the best-fit linear function ($y = ax + b$) to the data points. In this linear fit, $a = 0.006 \pm 0.001$ and $b = -0.379 \pm 0.003$ and $\sigma_{\log T} = 0.041$. $\sigma_{\log T}$ indicates the vertical data dispersion around the best-fit linear function in logarithm scale. $\sigma_{\log T} = 0.041$ corresponds to $\sim 10\%$ dispersion in linear scale.

conversion factor at 150 GHz to derive those at 98 and 220 GHz, assuming

$$T \propto \frac{S}{\text{FWHM}_{\text{PSF}}^2 (dB_{\nu}/dT)_{T_0}}, \quad (1)$$

where T is the differential CMB temperature, S is the flux density, and $(dB_{\nu}/dT)_{T_0}$ is the Planck function at the CMB temperature of $T_0 = 2.7255\text{K}$ (Fixsen 2009) and the observed frequency of ν_{obs} .

2.2.2. Source detection

The background-subtracted DR5 maps at 98, 150, and 220 GHz are utilized to detect new sources with Source-Extractor. The adopted aperture diameters are $1.0 \times \text{FWHM}_{\text{PSF}}$, corresponding to 2.1 , 1.3 , and 1.0 at 98 GHz, 150 GHz, and 220 GHz, respectively. These apertures take into account the different beam sizes for the different ACT bands. Therefore, the point-source aperture correction should be almost identical among the ACT bands, unless the beam shapes were to be significantly different. We adopt the same aperture correction (-0.379 dex) for the three ACT bands in this work.

The coordinates of the detected ACT DR5 sources are matched with those of our AKARI and IRAS samples, as

² We also follow the formula presented at <https://science.nrao.edu/facilities/vla/proposing/TBconv>

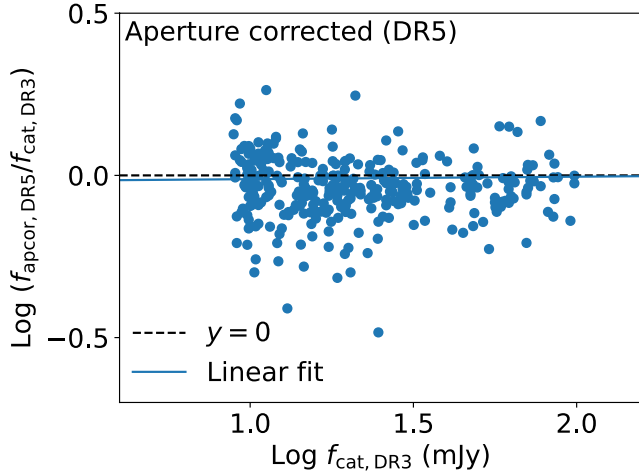


Figure 2. $\text{Log}(f_{\text{apcor,DR5}}/f_{\text{cat,DR3}})$ as a function of $\text{Log} f_{\text{cat,DR3}}$ for sources in the DR3 point-source catalog (Datta et al. 2019). Here, $f_{\text{apcor,DR5}}$ is the measured DR5 flux density corrected for aperture effect. $f_{\text{cat,DR3}}$ is the flux density in the DR3 point-source catalog. The observed frequency is 150 GHz for both DR3 and DR5. The horizontal dashed black line indicates $y = 0$, while the solid blue line is the best-fit linear function to the data points. Here, $a = 0.008 \pm 0.020$ and $b = -0.019 \pm 0.030$ and $\sigma_{\log f} = 0.096$. $\sigma_{\log f}$ indicates the vertical data dispersion around the best-fit linear function in logarithm scale. $\sigma_{\log f} = 0.096$ corresponds to $\sim 20\%$ dispersion in linear scale.

described in Section 2.1. The matching radius between the AKARI and ACT DR5 sources is $1.0 \times \text{FWHM}_{\text{PSF}}$ of the DR5 data, for each DR5 band. We use a $4'$ matching radius between the IRAS and ACT DR5 sources for all the DR5 bands, because the typical IRAS PSF size is $\sim 4'$ at $100 \mu\text{m}$ which is larger than those for ACT DR5. The background noises are estimated by random aperture photometries around matched sources. For each matched source and each band, we iterate 10,000 random aperture photometries around the source, to derive the standard deviation of the flux density, i.e., 1σ noise. The random aperture photometry provides 3σ upper limits of the source flux densities, if they are not detected in one or two ACT bands.

After the visual inspection, 101, 135, and 61 sources are found to match with the IRAS–AKARI sample with the signal-to-noise ratio (S/N) > 5 at 98, 150, and 220 GHz, respectively. In total, 167 galaxies are detected at any ACT frequency with $S/N > 5$, with 39 galaxies being detected with $S/N > 5$ at all three DR5 frequencies. Moreover, 76 galaxies are detected at 98 GHz and 150 GHz. 39 galaxies are detected at 98 GHz and 220 GHz. 54 galaxies are detected at 150 GHz and 220 GHz. As an example, ACT detection images of four

of the galaxies that are detected in the three ACT bands are shown in Figure 3.

2.2.3. Aperture correction for spatially extended sources

The aperture correction derived in Section 2.2.1 (-0.379 dex) is for ACT point sources. This correction could underestimate the flux densities of the spatially extended sources in the ACT images. To select such extended sources, we utilize the `FWHM_IMAGE` parameter (the FWHM of each source) measured by Source-Extractor. For the $S/N > 5$ sample in each ACT band, we estimate the standard deviation of the `FWHM_IMAGE` distribution (σ_{FWHM}). Spatially extended sources are selected if the `FWHM_IMAGE` are higher than $3\sigma_{\text{FWHM}} + \text{FWHM}_{\text{PSF}}$ in each ACT band. The thresholds are $4.2, 4.0$, and 4.3 at 98 GHz, 150 GHz, and 220 GHz, respectively. By applying these thresholds to the $S/N > 5$ samples, we identify 4, 7, and 3 extended sources at 98 GHz, 150 GHz, and 220 GHz, respectively.

We adopt optimized apertures for the spatially extended sources using “growth curves”, i.e., the total flux density within the aperture as a function of the aperture size. The flux densities are measured by using the optimized apertures for the extended sources, instead of applying the aperture correction of -0.379 dex (see §A for details).

2.2.4. Source matching with previous ACT extragalactic source catalogs

We crossmatch our IRAS–AKARI–ACT sample with the previous ACT extragalactic source catalogs of Mariage et al. (2011), Marsden et al. (2014), Datta et al. (2019), and Gralla et al. (2020). We use a matching radius based on the beam size of the relevant frequency, namely 1.3 for 150 GHz and 1.0 for 220 GHz. We have 5, 23, and 9 overlapping sources with the catalogs of Marsden et al. (2014), Datta et al. (2019), and Gralla et al. (2020), respectively. Since four sources among these are listed in both the catalogs of Datta et al. (2019) and Gralla et al. (2020), our sample includes 33 galaxies from these ACT catalogs. Therefore, compared to previous ACT extragalactic source catalogs, we have 134 new ACT-detected extragalactic sources in our sample.

We list the properties of the ACT-detected IRAS–AKARI IR galaxy sample in Table 1. Namely, we provide the IRAS/AKARI ID (column 1); the IRAS/AKARI coordinates (columns 2 and 3); the optical counterpart name (column 4); the redshift (column 5); the S/N at 98 GHz and $F_{98\text{GHz}}$ (columns 6 and 7); the S/N at 150 GHz and $F_{150\text{GHz}}$ (columns 8 and 9); the S/N at 220 GHz and $F_{220\text{GHz}}$ (columns 10 and 11); a note of a new ACT detection of the source in this work and a flag for extended sources (column 12);

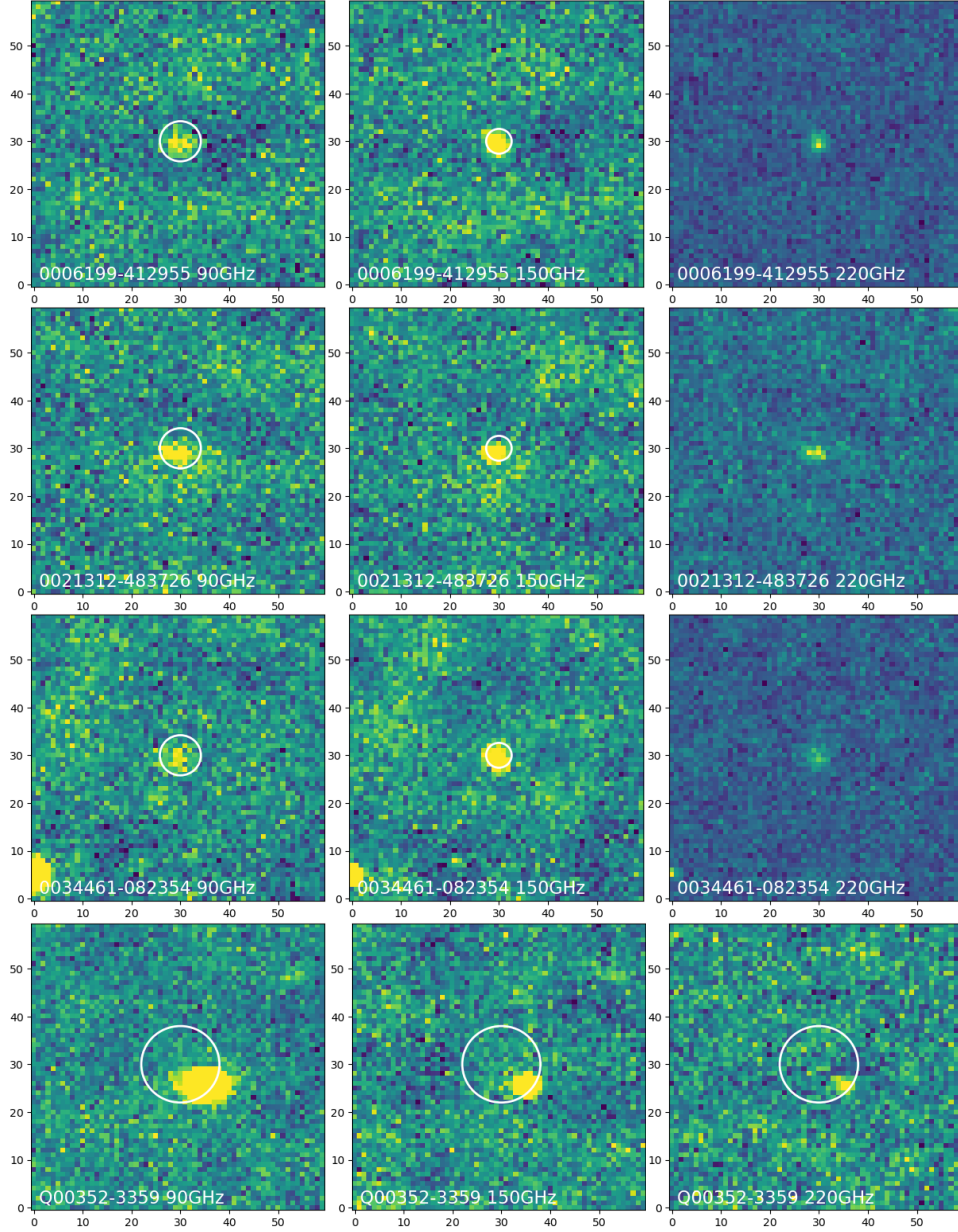


Figure 3. Example of ACT images of four of the sources (with $S/N \geq 5$) in our sample, detected at 98 GHz (left column), 150 GHz (middle column), and 220 GHz (right column), respectively. The source detections are shown inside the adopted searching radii (white circles) for matching. The image coordinates are provided in pixel units (1 pixel corresponds to $0''.5$). The first three rows indicate AKARI-matched ACT sources, while the bottom row shows an IRAS-matched ACT source. The center of each panel corresponds to the position of the AKARI or IRAS source.

and the radio detection information (column 13). Note that 12 ACT sources listed in Table 1 (AKARI/IRAS IDs 0215076-034302, 0529020-140507, 0727048-381415, Q00088-1449, L00125-3928, L00446-2101, Q05238-4602, 0610082+091503, 0626161+200221, 0854487+200629, 1058299+013401, and 1140184+174600) either do not have a reliable redshift measurement or have more than one counterpart candidate. Therefore, their optical counterpart and redshift entries are left empty.

As noted by Gralla et al. (2020), galaxies with $z \geq 0.05$ would be unresolved for the ACT beam size. Our sample includes a few galaxies at $z \sim 0.07$. A visual inspection of them indicates that they are local IR galaxies. Therefore, they are included in our sample for further analysis. Our sample also includes a couple of higher-redshift galaxies, at $z \sim 0.1$, which could be lensed systems. Since their number is low compared to

the local galaxies in our sample, we keep them in our sample for the SED analysis in §3.2.

Table 1. IRAS–AKARI IR galaxy sample detected by ACT.

AKARI/ ^a	R.A. ^b	Decl. ^b	Optical ^c	z^d	S/N^e	$F_{98\text{ GHz}}^f$	S/N^e	$F_{150\text{ GHz}}^f$	S/N^e	$F_{220\text{ GHz}}^f$	Note ^g	Radio ^h
IRAS	(J2000)	(J2000)	Counterpart		98	(mJy)	150	(mJy)	220	(mJy)		Reference
ID					GHz		GHz		GHz			
(1)	(2)	(3)	(4)	(5)	(6)	(7)	(8)	(9)	(10)	(11)	(12)	(13)
0006199-412955	1.58380	-41.49875	ESO 293-IG 034	0.0050	6	13.00 ± 2.01	15	26.88 ± 1.79	7	52.34 ± 6.91	*	
0009096-003659	2.29051	-0.61673	SDSS J000909.89-003705.3	0.0717			7	11.89 ± 1.58			1	
0010203-462510	2.58531	-46.41978	ESO 241-G 021	0.0203			5	9.85 ± 1.75	4		*	
Q00088-1449	2.85957	-14.55523			36	140.18 ± 3.84	26	109.06 ± 4.09	5	55.21 ± 10.53	*	i
L00125-3928	3.75411	-39.20403			5	105.65 ± 19.32	5	337.39 ± 58.42	5	1467.80 ± 254.74	*, E(98 GHz, 150 GHz)	
0021312-483726	5.38062	-48.62416	NGC 0092	0.0112	9	18.56 ± 1.94	12	21.38 ± 1.77	5	37.81 ± 6.58	*	
0023303+010053	5.87690	1.01450	WISEA J002329.14+010054.9	0.8286	10	25.52 ± 2.39	10	15.94 ± 1.53			1	
0029300-044140	7.37550	-4.69461	2MASX J00293024-0441350	0.0202	13	34.05 ± 2.47					*	i
0030227-331430	7.59520	-33.24195	NGC 0134	0.0053	5	25.95 ± 5.09	5	90.72 ± 17.80	13	96.37 ± 7.12	*, E(98 GHz, 150 GHz)	i
0034461-082354	8.69275	-8.39862	NGC 0157	0.0056	5	15.01 ± 2.64	12	24.24 ± 1.88	5	54.13 ± 10.25	1	

NOTE—A machine-readable version of the full Table 1 is available. A portion is shown here for guidance regarding its form and content.

^a AKARI ID as listed by the AKARI/FIS all-sky survey bright source catalog version 2.; IRAS ID from the IRAS PSCz (Saunders et al. 2000).

^b AKARI coordinates from the AKARI/FIS all-sky survey bright source catalog version 2.; IRAS coordinates from IRAS PSCz (Saunders et al. 2000).

^c Optical counterpart name from NED; empty if there is more than one counterpart candidate within the matching radius.

^d Redshift of the optical counterpart from the SDSS Data Release 17, 6dFGS, 2MASS, or IRAS PSCz spectroscopic redshift catalogs; empty if the redshift measurement is not reliable.

^e Measured S/N of the source in the map of the given frequency.

^f Measured flux density and its uncertainty from the map of the given frequency.

^g The “*” symbol indicates the galaxies that have new ACT identifications, as reported in this work. References for the previous ACT extragalactic source catalogs: (1) Datta et al. (2019); (2) Marsden et al. (2014); and (3) Gralla et al. (2020). “E” is a flag indicating that a source is extended, with a more than 3σ FWHM IMAGE size than the nominal PSF size at the noted band.

^h The radio catalog references are: (i) Condon et al. (1998); (ii) van Velzen et al. (2012); (iii) Helfand et al. (2015); and (iv) Murphy et al. (2010).

2.3. Multiwavelength Data of ACT-detected IRAS-AKARI IR Galaxy Sample

For the SED analysis in §3.2 we collect the UV, optical, near-IR, mid-IR, FIR and submillimeter archival flux densities of the counterparts, when available. The Galaxy Evolution Explorer (*GALEX*; Martin et al. 2005) scanned all the sky in the near-UV (NUV; $\lambda_{\text{eff}} = 2267\text{\AA}$) and far-UV (FUV; $\lambda_{\text{eff}} = 1516\text{\AA}$) bands. We use the Barbara A. Mikulski Archive for Space Telescopes Portal³ to match the optical counterpart positions of our sample within $5''$ with the *GALEX* source catalog (Martin et al. 2005), Data Release 6/7, and find 77 matches. We eliminate any unreliable measurements (NUV/FUV_ARTIFACT = 4, 64) and select the longest duration, if multiple measurements are listed for any source. *GALEX* photometry is corrected for Galactic foreground extinction using the listed E_{B-V} values (based on the extinction maps of Schlegel et al. 1998) in the *GALEX* source catalog.

We get the Galactic extinction-corrected u -, g -, r -, i -, and z -band magnitudes from the SDSS (York et al. 2000) Data DR17 (Abdurro'uf et al. 2022) *PhotoObjAll* catalog⁴. After avoiding unreliable photometry, with a CLEAN = 0 flag, we use SDSS photometry only for 13 sources in SDSS DR17. Since the available SDSS photometry is very limited, in order to include more optical counterpart photometry, our sample is crossmatched (within a search radius of $5''$) with the second data release (DR2) of the SkyMapper Southern Survey (SMSS; Onken et al. 2019), to include more optical counterpart photometry. SMSS (Wolf et al. 2018), which covers the entire southern sky, provides optical photometry in six bands: u , v , g , r , i , and z . We use $5''$ diameter aperture photometry in six bands from the DR2 photometry table⁵ for 86 matched galaxies in our sample. We consider only the reliable measurements, with FLAGS < 4 and NIMAFLAGS < 5. We use the given formalism in Casagrande et al. (2019) to convert the SMSS magnitudes to the band fluxes. We deredden the SMSS photometry in six bands, with the E_{B-V} values from Schlegel et al. (1998), as listed in the DR2 master table⁵, based on the Cardelli et al. (1989) extinction law.

For the 161 sources that have cross-identifications (within $3''$ of the optical counterpart position) in the 2MASS Point Source Catalog (Cutri et al. 2003; Skrutskie et al. 2003) and the 2MASS Extended Source Cat-

alog (2MASS XSC; Jarrett et al. 2000; Two Micron All Sky Survey Science Team 2020), we use the J -, H -, and K_s -band magnitudes. From 2MASS XSC, we use isophotal fiducial elliptical aperture magnitudes (20mag/sq.) for 102 sources. For the remaining 59 sources, we use the default magnitudes from the 2MASS Point Source Catalog. We use reliable photometry, without any artifact contamination and/or confusion flags (*cc_flags*). We apply Galactic reddening correction to the 2MASS magnitudes, based on the Schlegel et al. (1998) maps and the extinction law of Cardelli et al. (1989).

The AllWISE Source Catalog⁶ (Wright, Edward L. et al. 2019) lists the photometric measurements that have been obtained by the WISE all-sky survey in the $w1$ (centered at $3.4\mu\text{m}$), $w2$ (centered at $4.6\mu\text{m}$), $w3$ (centered at $12\mu\text{m}$), and $w4$ (centered at $23\mu\text{m}$) mid-IR bands (Cutri et al. 2021). The optical counterpart coordinates from our sample are crossmatched with the AllWISE Source Catalog within a $5''$ search radius. Of the available WISE photometry for 128 sources, we only use reliable measurements—with zero *cc_flags* values (*cc_flags* = '0000'), to avoid contaminated measurements; without high scattered moonlight contamination (i.e., 'moon_lev' < 5); with an S/N level greater than 2, not to include upper limits; with quality flag ($w1, 2, 3, 4\text{flg}$) values between 1 and 32, not to use upper limits; and without *null* uncertainties, to avoid upper limits or no measurements. The elliptical aperture magnitudes ("*wngmag*", where n is the band number) are used for the extended sources (with *ext_flg* > 0).

We obtain the AKARI mid-IR photometry in the 9 and $18\mu\text{m}$ bands from the AKARI/IRC all-sky survey point-source catalog, version 1⁷ (AKARI Team 2020), by crossmatching the AKARI/FIS coordinates within $20''$. For the AKARI FIR photometry in the 65, 90, 140, and $160\mu\text{m}$ bands, we use the AKARI/FIS all-sky survey bright source catalog, version 2 (Yamamura et al. 2018). In order to use reliable AKARI data, we only include the photometric measurements of high quality (*FQUAL* = 3).

For the 31 galaxies that are only detected by IRAS, we use the good-quality flux densities (with the flux quality flag 2 or 3) at 12, 25, 60, $100\mu\text{m}$, from the PSCz survey catalog (Saunders et al. 2000). We also use the upper limit on the flux density, given by a quality flag of 1.

³ <http://mast.stsci.edu>

⁴ <https://skyserver.sdss.org/dr17/>

⁵ <http://skymapper.anu.edu.au/table-browser/>

⁶ <http://wise2.ipac.caltech.edu/docs/release/allwise/>

⁷ http://www.ir.isas.jaxa.jp/AKARI/Observation/PSC/Public/RN/AKARI-IRC_PSC_V1_RN.pdf

The Herschel (Pilbratt et al. 2010) Photodetector Array Camera and Spectrometer (PACS; Poglitsch et al. 2010) performed FIR measurements at 70, 100, and 160 μm , while SPIRE (Griffin et al. 2010) performed submillimeter measurements at 250, 350 and 500 μm . In order to include Herschel photometry in our analysis, we crossmatch (within $5''$) the optical counterpart coordinates of our sample with the galaxy samples of Viero et al. (2014) and Clark et al. (2018). In total, we find Herschel counterparts for 23 sources. When available, we include the Herschel SPIRE measurements of these sources in our analysis. Since the AKARI FIR bands already cover the Herschel PACS bands, we only use Herschel PACS photometry for one source, for which the AKARI 90 μm photometry is not of good quality.

To account for the IR emission measurement discrepancies between the galaxies, due to the spatial resolution differences among IRAS, AKARI, WISE, and Herschel, we follow Clements et al. (2019) and apply their beam corrections that depend on the extendedness parameter (see equation 2 of Clements et al. 2019) to AKARI 65 μm and 90 μm measurements. To be conservative about the small beam size differences between AKARI/IRC ($9''$, Ishihara et al. 2010) and WISE ($6''$ – $12''$; Wright et al. 2010) we measure the mean difference between the two closest pairs of bands—namely, between the AKARI/IRC 9 μm and WISE 12 μm and the AKARI/IRC 18 μm and WISE 22 μm fluxes. We add the typical flux difference of $\sim 25\%$ in quadrature to the photometric uncertainties of the 9 μm , 12 μm , 18 μm , and 22 μm fluxes.

2.4. Radio Identification of ACT-detected IRAS–AKARI IR Galaxy Sample

We make use of the available radio galaxy catalogs of Condon et al. (1998), van Velzen et al. (2012), Helfand et al. (2015), Kuźmicz et al. (2018), and Murphy et al. (2010) to check the radio identifications of the galaxies in our sample. To identify the radio counterparts, we match the optical positions with the optical (or radio) counterpart coordinates listed in the investigated catalogs, within $20''$. We find radio identifications at $\nu = 1.4$ GHz for 106, 23, and 48 galaxies from the catalogs of Condon et al. (1998), van Velzen et al. (2012) and Helfand et al. (2015), respectively. Once the common sources in the different catalogs have been taken into account, a total of 113 galaxies in our sample have radio identifications at $\nu = 1.4$ GHz. Nine galaxies have radio identifications in the AT20G source catalog (Murphy et al. 2010), at $\nu = 20$ GHz. Eight of these galaxies had already been identified within the $\nu = 1.4$ GHz sample. We mark the galaxies with radio identifications

(now 114 in total) in Table 1 (column 13), with their references.

3. ANALYSIS AND RESULTS

3.1. Spectral indices

Millimeter-wave spectral indices can be used to determine the emission mechanism of the galaxy. AGN or dust-dominated sources can be designated from the 150–220 GHz spectral index. While synchrotron radiation powered by AGNs generates a negative α (less than unity), thermal dust-dominated radiation has α values greater than 2 (Hall et al. 2010; Mocanu et al. 2013; Marsden et al. 2014; Gralla et al. 2020). We compute millimeter-wave spectral indices of our IR galaxy sample over available frequency intervals—namely α_{98-150} , α_{98-220} , and $\alpha_{150-220}$ —from the listed flux densities in Table 1, as $\alpha_{\nu_2-\nu_1} = \log(F_2/F_1)/\log(\nu_2/\nu_1)$. We list the millimeter-wave spectral indices in Table 2.

When available, we classify each source, based on the $\alpha_{150-220}$ and α_{98-150} spectral indices, as a DSFG or synchrotron-dominated AGN. Our sample includes seven AGNs and 27 DSFGs among the 34 sources with available $\alpha_{150-220}$ and α_{98-150} . This is consistent with our initial selection of the galaxies in our sample as dusty IR sources. The distributions of the spectral indices of our sample are shown in Fig. 4. As seen in this figure, the DSFGs in our sample have spectral indices between: (i) $0.11 \leq \alpha_{98-150} \leq 3.71$; (ii) $0.55 \leq \alpha_{98-220} \leq 3.91$; and (iii) $0.16 \leq \alpha_{150-220} \leq 7.83$. The AGNs in our sample have spectral indices between: (i) $-1.43 \leq \alpha_{98-150} \leq -0.01$; (ii) $-1.29 \leq \alpha_{98-220} \leq -0.65$; and (iii) $-2.83 \leq \alpha_{150-220} \leq -0.99$. The median spectral indices of the DSFGs in our sample are: $\alpha_{98-150} = 0.75 \pm 0.65$; $\alpha_{98-220} = 1.56 \pm 0.73$; and $\alpha_{150-220} = 2.59 \pm 1.29$. The median spectral indices of the AGNs in our sample are: $\alpha_{98-150} = -0.40 \pm 0.35$; $\alpha_{98-220} = -1.04 \pm 0.20$; and $\alpha_{150-220} = -1.67 \pm 0.51$. The median spectral indices of $\alpha_{150-220} = 2.59 \pm 1.29$ obtained for the DSFGs in this work do agree (within uncertainties) with the reported values of 3.7 ± 0.6 by Marsden et al. (2014) and 3.7 ± 1.8 reported by Gralla et al. (2020).

3.2. SED Analysis

To model the SEDs of the IR galaxies from UV to millimeter wavelengths, it is necessary to combine the emissions from the different major components of these galaxies. The major emission components that contribute to the total luminosity of the IR galaxies are the SF, stellar population, dust, and AGN. The energy balance method (e.g., Efstathiou & Rowan-Robinson 2003; da Cunha et al. 2008; Noll et al. 2009; Boquien et al.

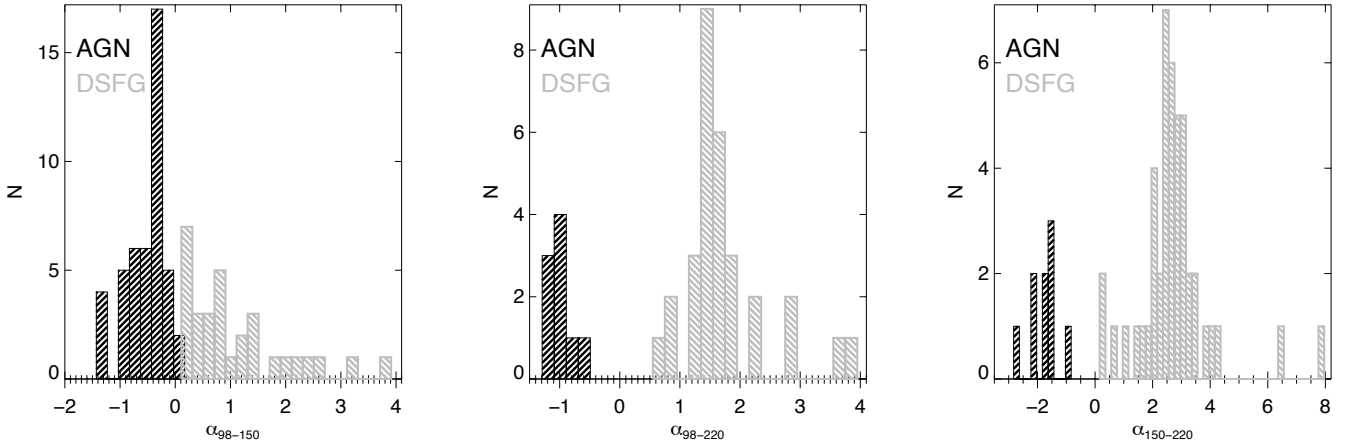


Figure 4. The distributions of the α_{98-150} (left), α_{98-220} (middle), and $\alpha_{150-220}$ (right) spectral indices. The black distributions represent galaxies that are classified as AGNs, according to the spectral indices, while the gray ones represent the galaxies that are classified as DSFGs.

Table 2. Spectral Indices of the IRAS–AKARI IR Galaxy Sample Detected by ACT. Only the sources with at least two ACT band detections and at least one spectral index available are listed.

Source ^a	α_{98-150} ^b	α_{98-220} ^b	$\alpha_{150-220}$ ^b	Type ^c	Type ^c
Name	α_{98-150} $\alpha_{150-220}$				
(1)	(2)	(3)	(4)	(5)	(6)
ESO 293-IG 034	1.4 ± 0.1	1.6 ± 0.0	1.7 ± 0.1	DSFG	DSFG
WISEAJ001126.18-143319.9	-0.5 ± 0.0	-1.0 ± 0.1	-1.8 ± 0.2	AGN	AGN
SSTSL2J001501.00-391216.9	2.3 ± 0.0	2.9 ± 0.0	3.8 ± 0.0	DSFG	DSFG
NGC 0092	0.3 ± 0.0	0.8 ± 0.0	1.5 ± 0.1	DSFG	DSFG
WISEAJ002329.14+010054.9	-0.9 ± 0.0				AGN
NGC 0134	2.5 ± 0.0	1.5 ± 0.1	0.2 ± 0.1	DSFG	DSFG
NGC 0157	0.9 ± 0.1	1.4 ± 0.0	2.1 ± 0.1	DSFG	DSFG
ESO 350-G040	-0.1 ± 0.0	-1.3 ± 0.0	-2.8 ± 0.1	AGN	AGN
UGC 00439	-1.2 ± 0.0				AGN
SSTSL2J004705.98-204459.4			7.8 ± 0.1	DSFG	

NOTE—Only the sources with at least two ACT band detections and at least one available spectral index are listed. A machine-readable version of the full Table 2 is available. Only a portion of this table is shown here for guidance regarding its form and content.

^a The optical counterpart name (when available) or the IRAS/AKARI ID, as listed in Table 1.

^b Spectral indices derived from the listed flux densities in Table 1 as $\alpha_{\nu_2-\nu_1} = \log(F_2/F_1)/\log(\nu_2/\nu_1)$.

^c Galaxy type, assigned from the specified spectral indices; AGNs are chosen for negative spectral indices, while DSFGs are chosen for positive values.

2019) is one of the main tools for modeling SEDs from UV to submillimeter wavelengths. Therefore, we use CIGALE (Noll et al. 2009; Serra et al. 2011; Boquien et al. 2019; Yang et al. 2022), version 2022.1 (Yang et al. 2022), for the SED fitting, based on the multiwave-

length data described in § 2.3. The broadband filters of the collected multiwavelength data are listed in Table 3. CIGALE⁸ is an ideal galaxy SED modeling tool for IR galaxies and AGNs (e.g., Malek et al. 2017; Vika et al. 2017; Jarvis et al. 2020), due to the energy conservation that is applied between the UV/optical emission that is then re-emitted by the dust in the IR. CIGALE models the unattenuated stellar component from the stellar population model and the star formation history (SFH). The attenuation is obtained for the given attenuation law, and the attenuated emission is then re-emitted in the IR. The emission components of the AGN (e.g., Fritz et al. 2006) and the synchrotron radiation in radio are then added. CIGALE creates a grid of precomputed model SEDs for each possible combination of the discrete parameters of each emission component (our user-defined parameters for each emission component model are listed in Table 4). The dimension of the grid depends on the user-defined parameters. CIGALE obtains the model fluxes after convolving the model SED with the filters. It computes the likelihood (corresponding to χ^2) of each model, by comparing the model fluxes with the observed fluxes. During the likelihood computing process, the models are scaled by a free scaling factor, to ensure extensive physical properties with acceptable values for the end product physical parameters, like the IR luminosity and the stellar mass, etc. In this Bayesian approach, the best-fitting SED is selected from the precomputed set of models, as the one with the lowest χ^2 , which is used as a maximum likelihood estimator.

⁸ <http://cigale.lam.fr/>

The Bayesian analysis of CIGALE employs the so-called pdf-analysis (Boquien et al. 2019), which evaluates the probability from the likelihoods (the lowest χ^2) of all the combined models of the stellar, dust, AGN, and radio synchrotron emission components and generates the probability distribution function (PDF) for each physical property (like the IR luminosity, dust mass, stellar mass, etc.). The finally obtained physical property and its uncertainty are the probability-weighted mean and standard deviation of its PDF. We note that in this SED fitting procedure, the obtained physical parameters are not always expected to be the unique possible values, because of the possible degeneracy between the input parameters. However, PDF distributions with a single peak ensure that the obtained physical parameters are reliable.

We use six modules to account for the different emission components in the SEDs. The stellar component of the SED is produced by the stellar population models, which are convolved with the adopted SFH model. In our analysis, we adopt the standard stellar population synthesis models of Maraston (2005), since they represent the near-IR stellar populations well (Maraston et al. 2009). These stellar population synthesis models are built from the Salpeter initial mass function (Salpeter 1955) with solar metallicity. Our sample of nearby galaxies ($z < 0.05$) have old stellar ages that cannot be well described with a constant SFH model. Therefore, we adopt the double exponentially declining SFH model SFH2EXP, in the form of a simple analytic function that is provided by CIGALE (Ciesla et al. 2015, 2016), which implements an SFH composed of two decreasing exponentials. We consider main stellar age values between 500 and 13,000 Myr. We use a large range of values for the e-folding time of the main stellar population model (τ_{main}), between 1 and 10,500 Myr. For the e-folding time of the late starburst population (τ_{burst}), we use values between 1 and 5000 Myr. We set the main stellar population age to be between 500 and 13,000 Myr. We use the age of the late burst between 1 and 1000 Myr. We note that most of the listed parameter values in Table 4 are chosen after several test runs of CIGALE.

We adopt the Charlot & Fall (2000) attenuation law for the dust attenuation, since it can account for different attenuation for young and old stars. In this attenuation law, there are two main attenuation sources: (i) the interstellar medium (ISM), which would affect both young and old stars (older than 10^7 yr); and (ii) the

Table 3. Photometric filters used in the SED analysis with CIGALE

Survey/Telescope	Filter	$\lambda_{\text{eff}} (\mu\text{m})$
GALEX	FUV	0.15
	NUV	0.23
SDSS	<i>u</i>	0.36
SMSS	<i>u</i>	0.35
SMSS	<i>v</i>	0.39
SDSS	<i>g</i>	0.46
SMSS	<i>g</i>	0.49
SMSS	<i>r</i>	0.60
SDSS	<i>r</i>	0.61
SDSS	<i>i</i>	0.74
SMSS	<i>i</i>	0.77
SDSS	<i>z</i>	0.89
SMSS	<i>z</i>	0.90
2MASS	<i>J</i>	1.24
	<i>H</i>	1.66
	<i>Ks</i>	2.16
WISE	W1	2.25
	W2	4.60
	W3	11.56
	W4	22.09
AKARI	S9W	9
	L18W	18
IRAS	IRAS1	12
	IRAS2	25
IRAS	IRAS3	60
	IRAS4	100
AKARI	N60	65
	WIDE-S	90.0
	WIDE-L	140.0
	N160	160.0
Herschel	PACS blue	68.927
	PACS red	153.95
Herschel	PSW	242.82
	PMW	340.89
	PLW	482.25
ACT	220 GHz	1362.69
	150 GHz	1998.61
	98 GHz	3059.11
VLA	1.4 GHz	214137.47

dust in the birth clouds, which would affect the young stars. The attenuations of these two sources are modeled by power laws. We use a combination of the allowed slope values for the ISM and birth clouds, as listed in Table 4. The dust model of Draine et al. (2014) is adopted for the dust component in the mid-IR and FIR regions. This model includes the mass fraction of polycyclic aromatic hydrocarbons (PAHs; q_{PAH}), with possible values between 0.47 and 7.32, and the minimum radiation field (U_{min} , with possible values between 0.1 and 50.0). The dust emission is in the power-law form of $dM_{\text{d}}/dU \propto U^{-\alpha}$ where M is the total dust mass and α is the slope within the 1–3 range. The γ represents

Table 4. Parameters Used in the SED fitting by CIGALE.

Parameter	Value
Double Exponential SFH (sfh2exp)	
Main stellar age [Myr]	500, 1000, 1050, 1500, 2000, 4000, 5000, 6000, 7200, 10,000, 10,400, 11,000, 11,300, 11,500, 12,000, 12,500, 13,000
Burst age [Myr]	1, 5, 10, 20, 50, 90, 100, 200, 800, 1000
τ_{main} [Myr]	1, 5, 10, 50, 100, 150, 200, 300, 350, 400, 700, 800, 1000, 2000, 10,500
τ_{burst} [Myr]	1, 5, 10, 20, 40, 45, 50, 100, 200, 300, 400, 700, 800, 5000
Dust Emission	
q_{PAH}	0.47, 1.12, 1.77, 2.50, 3.19, 4.58, 5.26, 5.95, 6.63
U_{min}	0.12, 0.15, 0.20, 0.35, 0.50, 0.60, 0.70, 0.80, 1.00, 1.20, 1.50, 1.70, 2.00, 2.50, 3.00, 3.50, 4.00, 5.00, 6.00, 7.00, 8.00, 10.00, 12.00, 17.00, 20.00
α	1.9, 2.0, 2.1, 2.2, 2.3, 2.4, 2.5, 2.8, 2.9, 3.0
γ	0.02, 0.1, 0.2, 0.7
Dust Attenuation Law	
Slope ISM	-0.7, -0.5, -0.4, -0.3, -0.1
Slope birth clouds	-1.3, -0.7, -0.5
AGN	
$R_{\text{max}}/R_{\text{min}}$	10, 30, 60, 100, 150
τ	0.1, 0.6, 1.0, 2.0, 3.0, 6.0, 10.0
β	-1.00, -0.75, -0.50, -0.25, 0.00
γ	0.0, 2.0, 4.0, 6.0
θ	60., 100., 140
ψ	0.001, 10.100, 20.100, 30.100, 40.100, 50.100, 60.100, 80.100, 89.990
frac_{AGN}	0.01, 0.02, 0.05, 0.09, 0.10, 0.15, 0.20, 0.25, 0.30, 0.35, 0.40, 0.50, 0.60
Synchrotron Radio Emission	
q_{IR}	2.4, 2.5, 2.58, 2.6, 2.7
α_{SF}	0.8
R_{AGN}	0, 0.01, 0.02, 0.1, 0.2, 1, 2, 3, 10, ..., 50, 100, 1000
α_{AGN}	0.3, 0.4, 0.5, 0.6, 0.7, 0.8, 0.9, 1.0

the fraction of the dust mass (between 0 and 1) that is heated by a greater radiation field than U_{min} . As suggested by Toba et al. (2020), we use different γ values, to obtain a better fit of the FIR emission. The modified Fritz et al. (2006) models are used for the AGN component. These include the isotropic point-like central source power-law radiation (in the 0.001–20 μm wavelength range) and the dust emission in a toroidal structure. In this model, dust (mainly silicate and graphite grains) can scatter the continuum radiation from the center or it can absorb and re-emit it at 1–1000 μm . The model includes three components: the central AGN, the scattered emission, and the thermal dust emission from the torodial structure. The size of the torodial structure is given by the ratio of the maximum outer radius to the minimum innermost radius ($R_{\text{max}}/R_{\text{min}}$), with allowed values between 10 and 150. The absorption feature of the silicate grains at 9.7 μm is taken into account by the optical depth parameter τ , which can have values of 0.1, 0.3, 0.6, 1.0, 2.0, 3.0, 6.0, or 10.0. The radiation of the torodial structure depends on the density distribution $r^\beta e^{-\gamma|\cos\theta|}$, where β represents the radial dust distribution, with allowed values between -1 and 0, and γ represents the angular dust distribution, with allowed

values between 0.0 and 6.0. Here, θ is the opening angle of the torodial structure, with allowed values of 60°, 100°, or 140°. The ψ parameter is the angle between the equatorial axis and the line of sight, with allowed values between 0.001 and 89.990. While Type 1 AGNs have $\psi = 90^\circ$, a Type 2 AGN can have $\psi = 0^\circ$. We include most of the allowed parameter values of the Fritz et al. (2006) models, to include the models of different AGN types. The contribution of the fractional AGN emission total IR emission is shown by the frac_{AGN} parameter. In order to be able to model AGN components with different strengths (both low and high), we consider frac_{AGN} values starting from 0.0 to 0.6. The synchrotron radio emission includes two different model components: (i) the radio emission from the SF; and (ii) the AGN radio emission. The radio synchrotron emission produced by the SF is modeled as a cutoff power-law component, with a slope (α_{SF}), whose value of 0.8 is adopted as default parameter in our analysis. The radio–IR correlation coefficient, q_{IR} , which is the normalization of the SF radio emission (Helou et al. 1985) at 1.4 GHz, has a default value of 2.58 in CIGALE. Following Yang et al. (2022), we allow q_{IR} to vary between 2.4 and 2.7 in our analysis, to be consistent with the observations

conducted by [Delvecchio et al. \(2021\)](#). The AGN radio emission is modeled with a simple power-law component, between 0.1 and 1000 mm, with a slope $\alpha_{\text{AGN}} = 0.7$ ([Randall et al. 2012](#)). In our analysis, we allow α_{AGN} to be between 0.3 and 1.0, to have statistically reliable fits. The AGN radio emission model also includes the radio-loudness parameter R_{AGN} , which is the ratio of the monochromatic luminosities at 5 GHz and 2500 Å (e.g., Equation (9) of [Yang et al. 2022](#)). We allow R_{AGN} to have a large range, between 0 and 1000.

With the parameter settings listed in Table 4 and the available photometric data listed in Table 3, we model the stellar, AGN, and dust emission components, by using at most 39 photometric points from UV to radio wavelengths. In order to apply CIGALE, at least one detection at each of the UV–optical, near-IR, mid-IR, and FIR regions is required, to obtain an accurate model. To have a reliable dust SED, we also need detections at both the shorter and longer wavelengths of the SED peak near 100 μm . We also use the 3σ noise levels in each ACT band as the nondetection upper limits in the SED analysis. These criteria allow us to perform the SED analyses for 87 galaxies in our sample.

In the first run of CIGALE, we use only the stellar, AGN, and dust components, without the radio data at 1.4 GHz. After the first run, all the obtained SEDs are visually checked. In most of the SEDs, the millimeter-band fluxes are higher compared to the dust component. Based on the millimeter measurements, we see that more than half of our sample requires a radio component. Therefore, after the first run, the radio synchrotron emission component is added, to model the SEDs between the 100 μm and millimeter regions. We also quantify the FIR–millimeter wave color range that would require a radio component (see §3.3), based on our SED analysis.

Our main goals are to identify the origins of the millimeter emissions measured from the galaxies in our sample and to measure the physical parameters from the SEDs. Since the radio flux at 1.4 GHz is crucial in order to obtain a reliable fit for the synchrotron radio component, it is included in the further SED analysis, when available. As a result, we obtain statistically reliable (mostly $\chi^2_{\text{reduced}} \leq 5.0$, and only for a few cases $\chi^2_{\text{reduced}} \sim 8$) fits for 69 galaxies. Among these statistically reliable SEDs, 63 have a radio component, either because it has a radio detection at 1.4 GHz or because its millimeter data require one (these being higher than the FIR dust component). We divide these 63 SEDs into two groups, based on the radio-loudness parameter of the AGN: (i) radio-loud $R_{\text{AGN}} > 10$; and (ii) radio-quiet $R_{\text{AGN}} \leq 10$. In Figures 5 and 6, example SEDs

are shown for the radio-loud AGNs and the radio-quiet AGNs, respectively. There are radio SF galaxies among the radio-quiet AGNs whose AGN radio emissions are insignificant. We show example SEDs of these, as a third group, in Figure 7. Only six SEDs do not have a radio component, since the millimeter emission is consistent with the FIR dust emission, and they do not have a radio detection at 1.4 GHz. Figure 8 shows aexample SEDs for the cases where a radio synchrotron emission component is not required.

Our SED analysis shows that the millimeter data, which are usually lacking from galaxy SEDs, are highly valuable for accurately defining the SED shape, beyond the SED peak of around 100 μm . For our sample, the millimeter emission mostly originates (for more than half of our sample) from the AGN synchrotron radio radiation (and in these cases, the radio emission from the SF still has a contribution). For a quarter of the sample at least, the origin is the SF synchrotron radio radiation. And for a minor group, the origin is the FIR dust emission.

We measure the total IR luminosity $L(\text{IR})_{\text{TOTAL}}$ as the sum of L_{dust} and $L(\text{IR})_{\text{AGN}}$ from best-fitted SED model. We exclude four galaxies from this analysis, since the ACT millimeter data points do not fit well with the obtained best-fitting model. We separately quantify the relationships between the total IR luminosity, the AGN luminosity, and the millimeter-band luminosities at 98, 150, and 220 GHz for the 43 galaxies with AGN radio emission and the 16 SF radio galaxies, as shown in Figure 9. The adopted form of the investigated luminosity relationships is as follows:

$$\log(L(\text{IR})_{\text{TOTAL/AGN}}) = B + \alpha_{L\nu} \log(L_\nu) + \epsilon_{L\nu}. \quad (2)$$

where the zeropoint is B , the slope is α , the estimated scatter is ϵ and ν is the frequency. The Bayesian regression of ([Kelly 2007](#)) is used to obtain the best-fitting parameters. We list the obtained parameters in Table 5. As seen in Fig. 9, the 98 GHz, 150 GHz, and 220 GHz band luminosities measured from the SEDs are in similar ranges for both the AGN and SF radio galaxies. Compared to the SF radio galaxies, the AGN radio emission galaxies have a larger scatter around the best-fitting relationship. Therefore, their slopes are different, as listed in Table 5. We list the physical parameters measured from the SEDs in Table 6. We check the reliability of these physical parameters with a mock analysis in CIGALE. In this procedure, CIGALE takes the data of each galaxy, based on the best-fitting SED, and adds a noise computed from a Gaussian distribution with the same standard deviation as the observed data. The CIGALE analysis is repeated for this mock catalog,

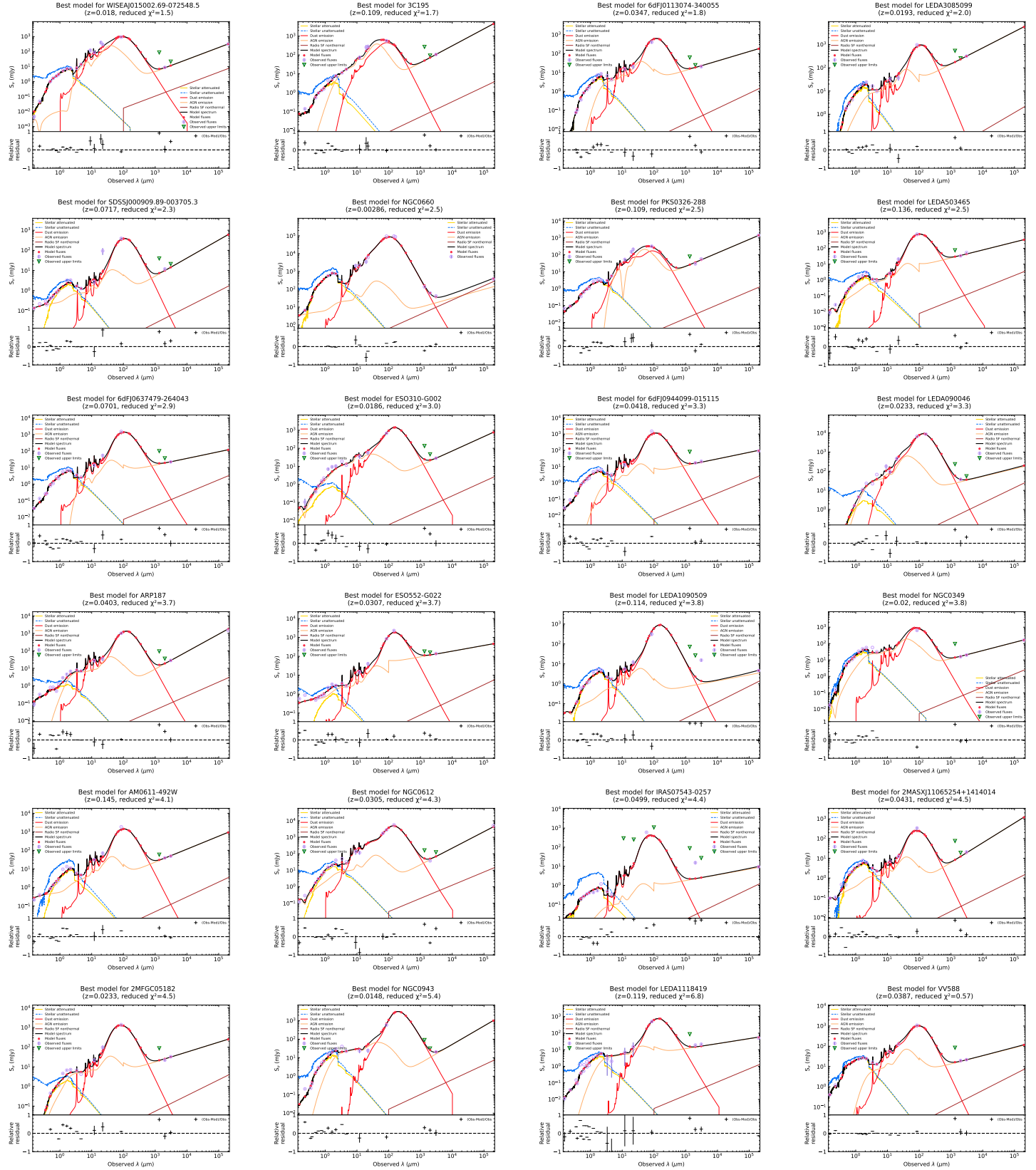


Figure 5. Best-fitting models of radio-loud AGNs in our sample. The observed fluxes and best-fitting model fluxes are shown by the open violet circles and the filled red circles, respectively. The unattenuated stellar emission, the dust emission, and the total AGN emission are shown by the dashed blue lines, the solid red lines, and the solid orange lines, respectively.

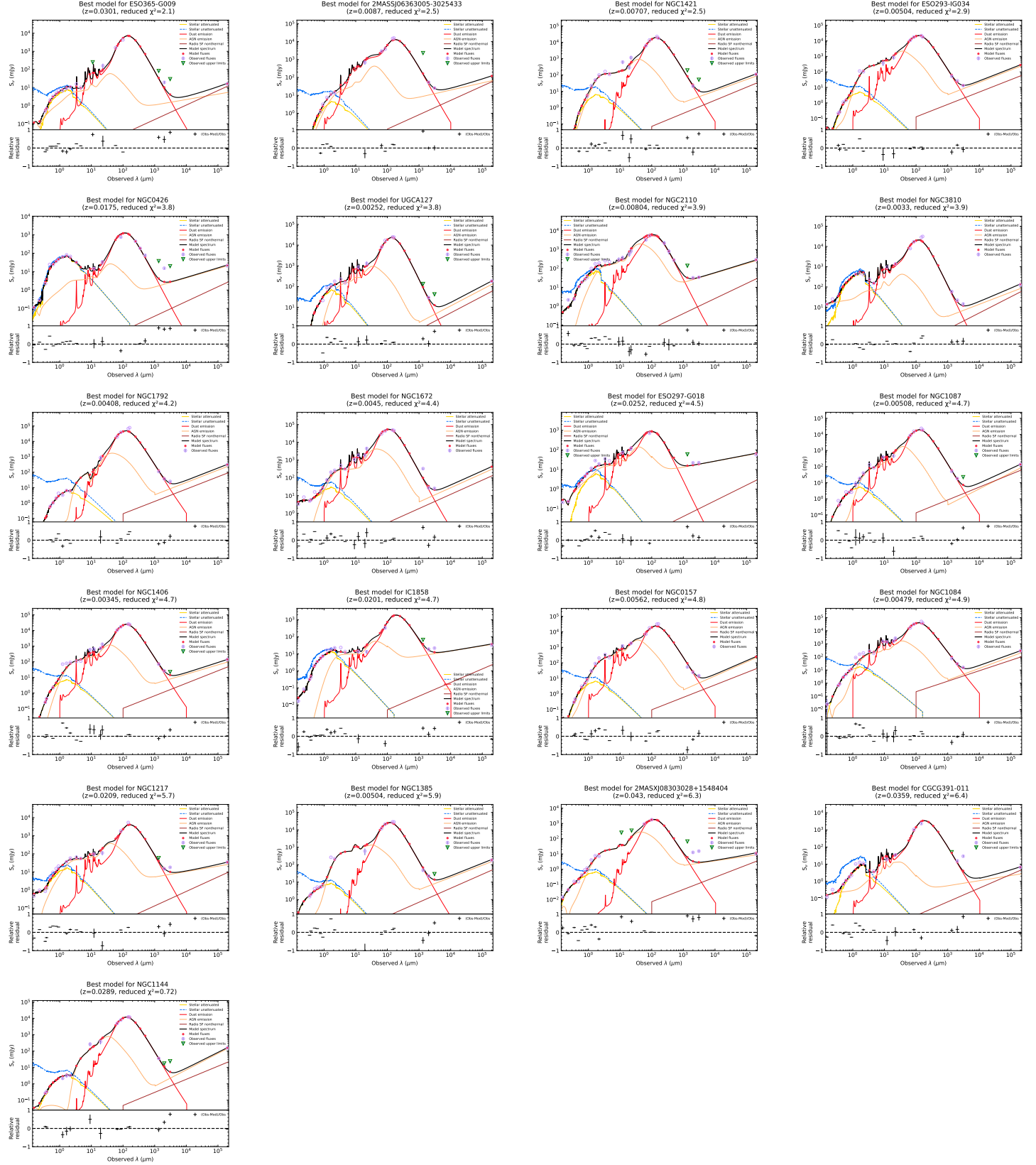


Figure 6. Best-fitting models of radio-quiet AGNs in our sample. The symbol styles for the flux values and the color codes for the different model components are the same as in Figure 5.

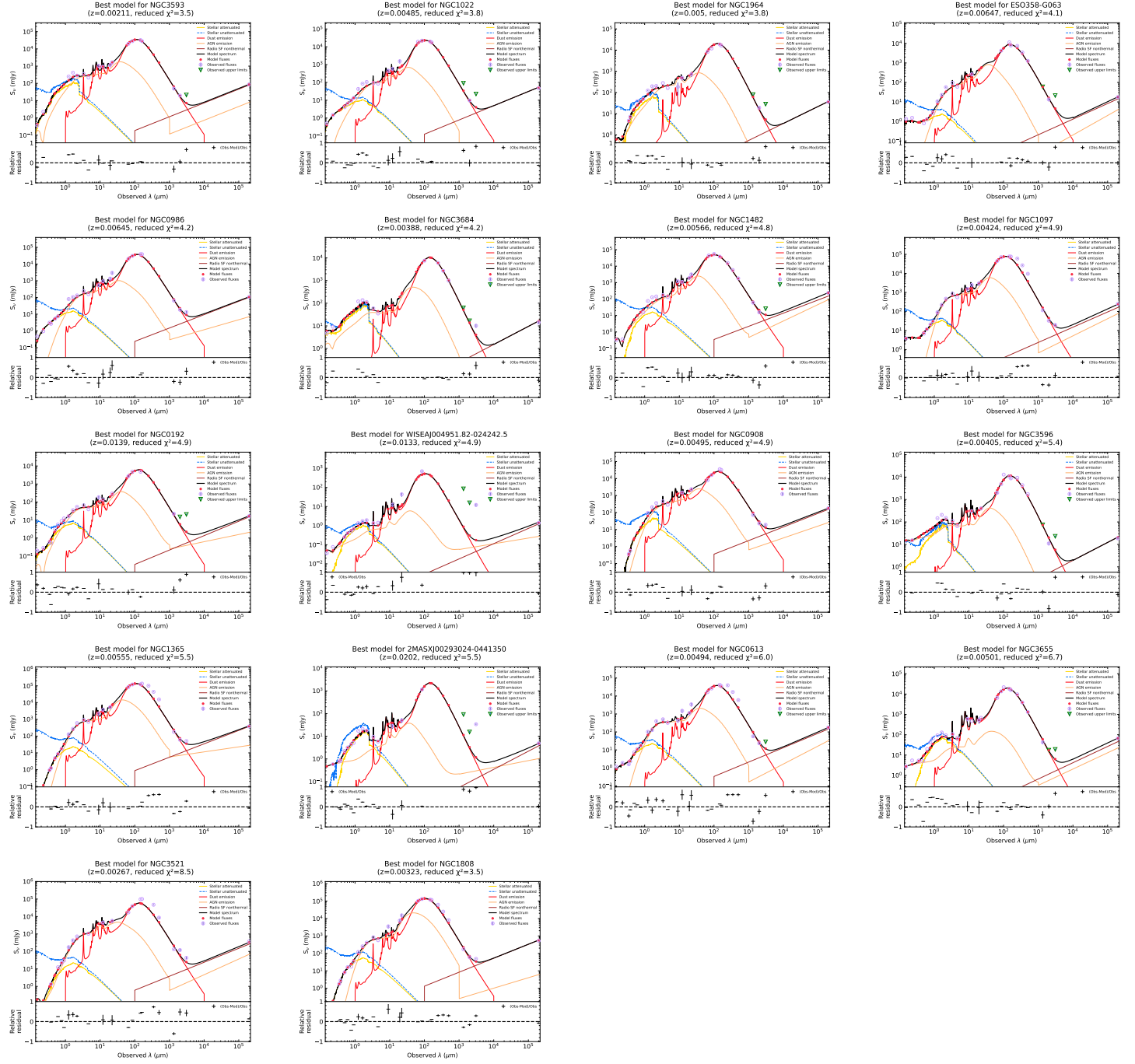


Figure 7. Best-fitting models of radio star-forming galaxies in our sample. The symbol styles for the flux values and the color codes for the different model components are the same as in Figure 5.

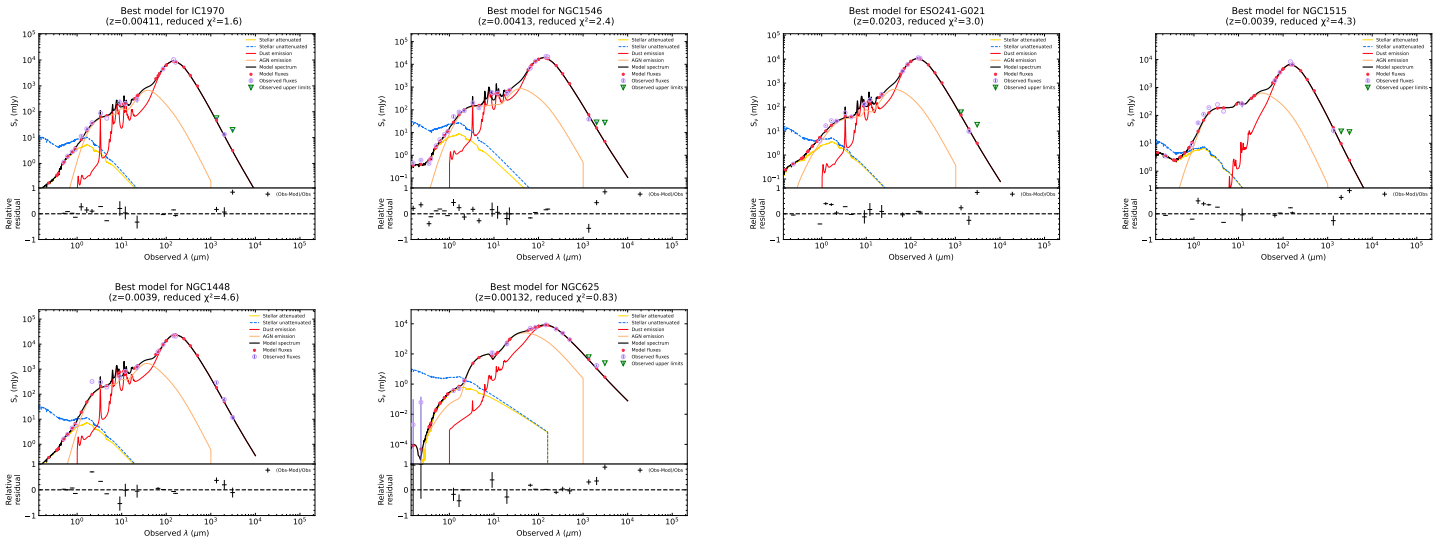


Figure 8. Best-fitting models of the galaxies for which the radio synchrotron emission component is not required in the SED, since the millimeter emission is consistent with the FIR dust emission and there is no radio detection at 1.4 GHz. The symbol styles for flux the values and the color codes for the different model components are the same as in Figure 5.

based on the same set of user-defined parameters that were used for the original analysis. The obtained physical parameters from the mock analysis correlate well with the parameters obtained from the original analysis.

3.3. FIR-to-Millimeter Wave and Millimeter-wave Color Distributions of Our Sample

We initially add the radio synchrotron emission component to the SEDs after visual inspection. This need and the origin of the millimeter radiation can be quantified by the FIR–millimeter wave colors, so we therefore check the possible color combinations for our sample. The color distributions for different galaxy groups are shown in Fig. 10. Here, the $\log(F_{90\,\mu\text{m}}/F_{98\,\text{GHz}})$ color distribution in the top left panel and the $\log(F_{90\,\mu\text{m}}/F_{150\,\text{GHz}})$ distribution in the top right panel similarly show that in the $\log(F_{90\,\mu\text{m}}/F_{98\,\text{GHz}}) < 2.0$ and $\log(F_{90\,\mu\text{m}}/F_{150\,\text{GHz}}) < 2.0$ ranges, radio-loud and radio-quiet AGNs contribute significantly to the millimeter radiation, and that the synchrotron emission component is therefore needed in the SEDs. Since our sample includes only a few sources with $\log(F_{90\,\mu\text{m}}/F_{220\,\text{GHz}})$ color, it is not large enough to determine a range for different distributions.

The millimeter color distributions of our sample are shown in the bottom panels of Fig. 10. Since our sample includes only a few SEDs with $F_{220\,\text{GHz}}$ detections, the color combinations including this band do not provide a reliable separation range (as in the bottom right), except for the clearly distinct region between $-1.4 < \log(F_{98\,\text{GHz}}/F_{220\,\text{GHz}}) < -1.2$, for the dust emission. The $\log(F_{98\,\text{GHz}}/F_{150\,\text{GHz}}) > 0.15$ region (bottom left) indicates a partial limit for radio-loud AGNs, while the $\log(F_{98\,\text{GHz}}/F_{150\,\text{GHz}}) > -0.4$ region requires a radio component in the SEDs.

3.4. Correlation Investigation of the FIR-to-Millimeter Wave and Millimeter-wave Colors

Any possible correlations between the physical parameters ($L(\text{IR})_{\text{TOTAL}}$, L_{dust} , $L(\text{IR})_{\text{AGN}}$, frac_{AGN} , and ψ_{AGN}) measured directly from the SEDs and the FIR-to-millimeter wave and millimeter-wave colors are investigated. For this investigation, we include the AGN parameters of all galaxies, as measured from the SEDs, without applying any criteria for the AGN selection. The strengths of the correlations are measured using the Spearman rank correlation coefficient (r_s). As

a result, we only find moderate correlations between $\log(L(\text{IR})_{\text{dust}})$ and the $\log(F_{98\,\text{GHz}}/F_{150\,\text{GHz}})$ color ($r_s = 0.54$, with a significance⁹ of 0.002) and $\log(L(\text{IR})_{\text{TOTAL}})$ and the $\log(F_{98\,\text{GHz}}/F_{150\,\text{GHz}})$ color ($r_s = 0.63$, with a significance of 0.0003), as shown in Fig. 11. These moderate correlations can be used as crude estimates for L_{dust} and $L(\text{IR})_{\text{TOTAL}}$ from the millimeter-wave colors, in the absence of redshift information.

4. DISCUSSION

4.1. Comparison with Previous Work on Millimeter-selected Galaxies

As reported by the previous studies of millimeter-selected galaxies (e.g., Planck Collaboration and Aalto et al. 2011; Gralla et al. 2020), using ACT or Planck, a subset of these galaxies are DSFGs. Among those DSFGs, most sources are high-redshift lensed galaxies, while others are low-redshift star-forming IR galaxies. The main focuses of the earlier work on these low-redshift millimeter-selected IR galaxies have been detections in the millimeter maps, counterpart identifications, measuring the flux densities for the ACT bands, obtaining ACT spectral indices from the multifrequency data, and source classification (AGN/DSFG), based on the spectral indices (e.g., Marriage et al. 2011; Marsden et al. 2014; Datta et al. 2019; Gralla et al. 2020).

In §3.1, we computed millimeter-wave spectral indices and compared the sample mean values with the values that have been given by Marsden et al. (2014) and Gralla et al. (2020). Although our sample size is much smaller than theirs (less than a quarter of their sample sizes), our median value of $\alpha_{150-220} = 2.59 \pm 1.30$ (which is computed from the two overlapping ACT bands with their studies) is lower compared to their reported values (although it agrees within the sample standard deviation).

The SEDs of ACT-detected millimeter DSFGs have also been investigated in previous studies, by including FIR data (e.g., Su et al. 2017; Gralla et al. 2020). However, these studies only examined the SEDs of high-redshift lensed DSFGs. Therefore, we cannot make a direct comparison between the SEDs of low-redshift IR galaxies analyzed in this work and those studies.

4.2. Implications of Including ACT Millimeter Bands in the SEDs

⁹ The significance values show that there is less than a 0.1% chance that the found r_s occurred by chance, if there were no correlations between these parameters.

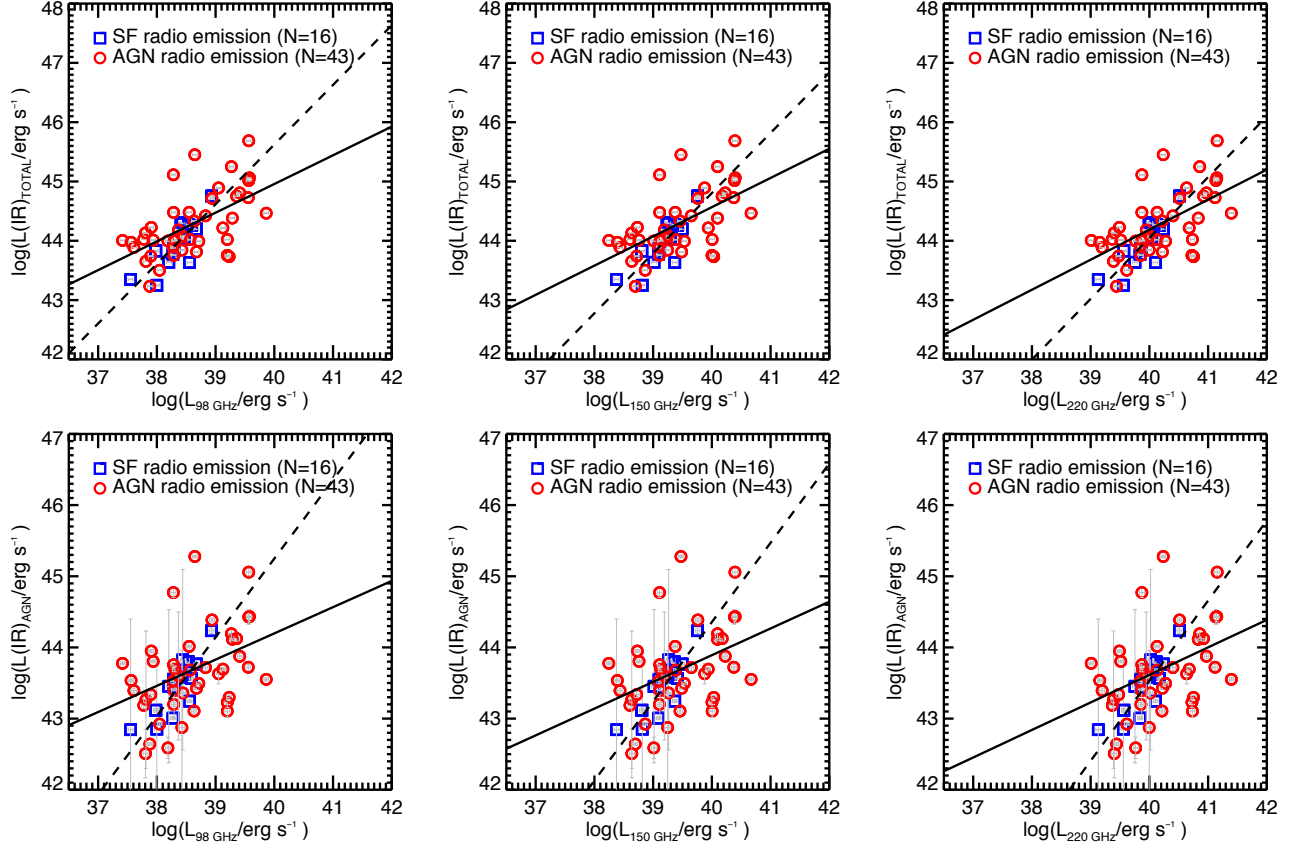


Figure 9. The total IR luminosity (top) and the AGN luminosity (bottom) vs. the millimeter-band luminosities measured from the SED model at 98 GHz (left), 150 GHz (middle), and 220 GHz (right) for the 43 galaxies with AGN radio emission (red circles) and the 16 SF radio galaxies (blue squares). These relationships can be used to estimate the AGN and total IR luminosities from the millimeter-band luminosities. The solid lines represent the relationships for the AGN radio emission, while the dashed lines show the relationships for the SF radio emission.

Table 5. Parameters of the Relationships between the Total IR Luminosity, AGN Luminosity, and the Millimeter-band Luminosities at 98, 150, and 220 GHz.

Luminosities	$\alpha_{L_{\nu} \text{ GHz}}$	B	$\epsilon_{L_{\nu} \text{ GHz}}$
$\log(L(\text{IR})_{\text{TOTAL}}) - \log(L_{98 \text{ GHz}})$ AGN radio emission	0.48 ± 0.11	25.60 ± 4.35	0.46
$\log(L(\text{IR})_{\text{TOTAL}}) - \log(L_{98 \text{ GHz}})$ SF radio emission	1.01 ± 0.23	5.39 ± 8.68	0.26
$\log(L(\text{IR})_{\text{TOTAL}}) - \log(L_{150 \text{ GHz}})$ AGN radio emission	0.49 ± 0.11	24.85 ± 4.44	0.46
$\log(L(\text{IR})_{\text{TOTAL}}) - \log(L_{150 \text{ GHz}})$ SF radio emission	1.01 ± 0.22	4.24 ± 8.70	0.25
$\log(L(\text{IR})_{\text{TOTAL}}) - \log(L_{220 \text{ GHz}})$ AGN radio emission	0.51 ± 0.11	23.93 ± 4.53	0.45
$\log(L(\text{IR})_{\text{TOTAL}}) - \log(L_{220 \text{ GHz}})$ SF radio emission	1.03 ± 0.22	3.00 ± 8.60	0.24
$\log(L(\text{IR})_{\text{AGN}}) - \log(L_{98 \text{ GHz}})$ AGN radio emission	0.36 ± 0.14	29.67 ± 5.50	0.57
$\log(L(\text{IR})_{\text{AGN}}) - \log(L_{98 \text{ GHz}})$ SF radio emission	1.10 ± 0.32	1.25 ± 12.30	0.23
$\log(L(\text{IR})_{\text{AGN}}) - \log(L_{150 \text{ GHz}})$ AGN radio emission	0.37 ± 0.14	29.09 ± 5.64	0.57
$\log(L(\text{IR})_{\text{AGN}}) - \log(L_{150 \text{ GHz}})$ SF radio emission	1.11 ± 0.32	0.01 ± 12.42	0.23
$\log(L(\text{IR})_{\text{AGN}}) - \log(L_{220 \text{ GHz}})$ AGN radio emission	0.38 ± 0.14	28.37 ± 5.78	0.57
$\log(L(\text{IR})_{\text{AGN}}) - \log(L_{220 \text{ GHz}})$ SF radio emission	1.12 ± 0.31	-1.28 ± 12.43	0.22

Table 6. Physical parameters of 69 IR galaxies measured from the statistically reliable SED analysis with CIGALE.

Optical Counterpart	$\log(L(\text{IR})_{\text{TOTAL}}$	$\log(L_{\text{dust}}$	$\log(M_{\text{dust}}$	$\log(L(\text{IR})_{\text{AGN}})$	frac_{AGN}	ψ_{AGN}	Origin of	α_{AGN}	R_{AGN}
Name	/ erg s ⁻¹	/ erg s ⁻¹	/ kg)	/ erg s ⁻¹	Millimeter Emission				
(1)	(2)	(3)	(4)	(5)	(6)	(7)	(8)	(9)	(10)
ESO293-IG034	43.90 ± 0.01	43.66 ± 0.01	37.65	43.52 ± 0.03	0.35	20.10	2	0.80	1
SDSSJ000909.89-003705.3	44.48 ± 0.01	44.30 ± 0.01	37.83	44.01 ± 0.02	0.10	89.99	1	0.80	1000
ESO241-G021	44.64 ± 0.01	44.50 ± 0.01	38.82	44.05 ± 0.02	0.20	30.10	4	.00	
2MASXJ00293024-0441350	43.98 ± 0.01	43.83 ± 0.01	38.20	43.46 ± 0.02	0.10	80.10	3	0.30	1
NGC0157	44.02 ± 0.01	43.75 ± 0.01	37.99	43.68 ± 0.02	0.40	30.10	2	0.90	1
NGC0192	44.20 ± 0.01	44.00 ± 0.01	38.07	43.77 ± 0.03	0.25	30.10	3	0.40	0
WISEAJ004951.82-024242.5	43.05 ± 0.01	42.98 ± 0.01	36.52	42.21 ± 0.02	0.05	50.10	3	0.30	1
NGC0349	44.01 ± 0.01	43.62 ± 0.01	36.61	43.78 ± 0.02	0.45	30.10	1	0.60	11
NGC0426	43.66 ± 0.01	43.55 ± 0.01	37.29	43.00 ± 0.08	0.10	40.10	2	0.50	9
6dFJ0113074-340055	44.00 ± 0.01	43.87 ± 0.01	37.63	43.39 ± 0.39	0.20	20.10	1	0.60	100

NOTE— The number codes for the origins of the millimeter emission are as follows: (1) Radio-loud AGN; (2) Radio-quiet AGN; (3) SF radio galaxy; (4) and dust emission. A machine-readable version of the full Table 6 is available. Only a portion of this table is shown here for guidance regarding its form and content.

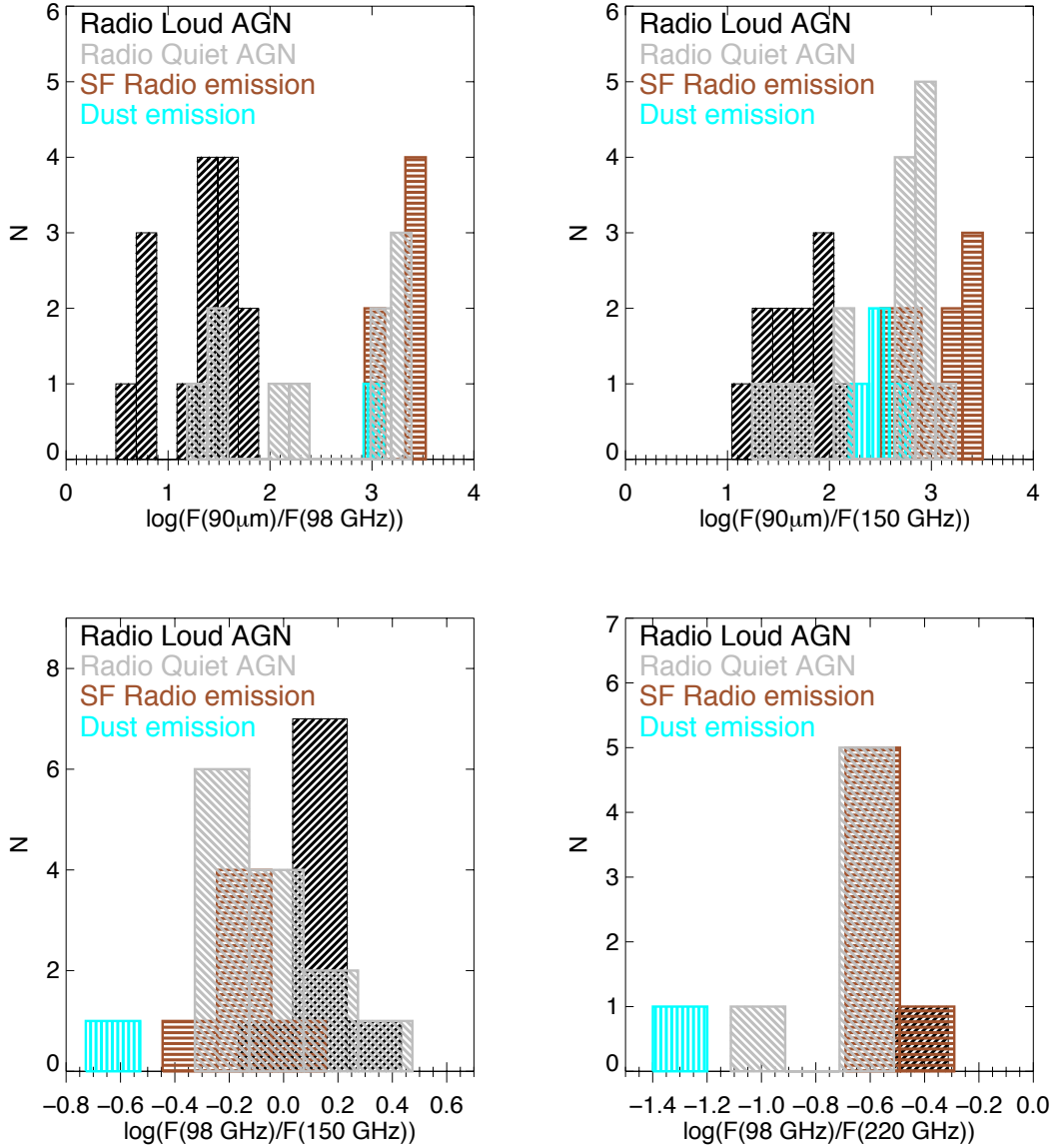


Figure 10. The $\log(F_{90\mu\text{m}}/F_{98\text{ GHz}})$ (top left), $\log(F_{90\mu\text{m}}/F_{150\text{ GHz}})$ (top right), $\log(F_{98\text{ GHz}}/F_{150\text{ GHz}})$ (bottom left) and $\log(F_{98\text{ GHz}}/F_{220\text{ GHz}})$ (bottom right) color distributions of our sample. The black distribution represents the radio-loud AGNs, the gray one represents the radio-quiet AGNs, the brown one represents the SF radio galaxies, and the cyan one represents the dust emission. These color distributions are extremely useful for estimating the origins of the millimeter radiation, based only on the observed color, without any redshift requirement.

When the traditional UV-to-FIR SEDs expand to millimeter wavelengths, depending on the FIR-to-millimeter-wave and/or millimeter flux ratios, namely the colors, a radio synchrotron emission component is needed to obtain a valid SED model. Such color limits are determined in §3.3. As a following investigation, we check the color distributions of the sources with different origins. As shown in Figure 10, the color distributions for the dust, SF, and AGN emission show differences.

Therefore, the color range that we obtained in §3.3 can be used as a crude indication of the different origins of millimeter-band detections. However, it is valid to clearly separate the dust emission and radio synchrotron component from the AGN and/or SF.

We emphasize that the minor group of dust emission-originating millimeter emission galaxies constitute very important representatives of high-redshift star forming galaxies, which are our best tools for investigating these

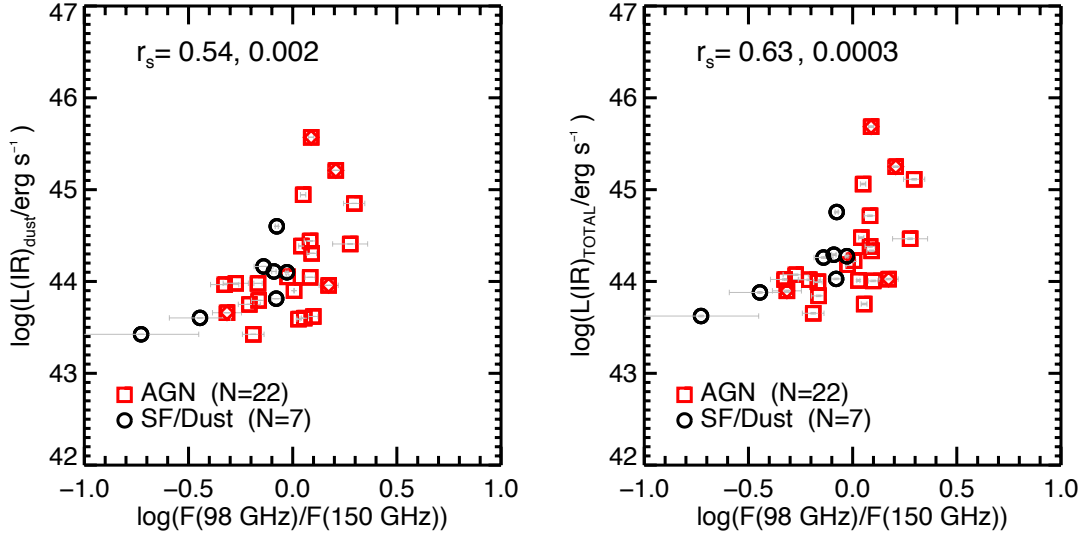


Figure 11. The physical parameters L_{dust} and $L(\text{IR})_{\text{TOTAL}}$ measured from the SEDs vs. the $F_{98\text{ GHz}}/F_{150\text{ GHz}}$ color. The red squares represent the AGNs and the black circles represent the SF galaxies. The Spearman rank correlation coefficient values r_s are listed, with significances of 0.002 (left) and 0.0003 (right).

DSFGs beyond redshift $z = 2$. Additionally, our SF radio galaxy group shows that radio emission does not necessarily mean significant AGN contamination in the millimeter band, as such galaxies at higher redshifts should be considered as being SF-dominated. We recommend obtaining an SED decomposition for this type of galaxy.

4.3. Future Prospects with JWST

The James Webb Space Telescope (JWST) has unique capabilities in terms of observing the near-IR to mid-IR emission from these IR galaxies. For example, four nearby IR galaxies have already been selected for inclusion in the Director’s Discretionary Early Release Science Program #1328. These IR galaxies are not in our sample, but their observations will show the full potential of JWST MIRI and NIRSpec observations, which will observe the IR SEDs in detail, by separating the IR dust continuum emission lines, like PAHs and other atomic and molecular emission lines. Most importantly, it will be possible to detect the AGN components in the mid-IR spectra obtained by JWST. Therefore, IR galaxies that have a radio component, as revealed by the millimeter data with small AGN fractions (obtained from our SED analysis), may reveal their possibly hidden AGNs by JWST.

5. CONCLUSIONS

We search for the millimeter counterparts of IR galaxies selected by AKARI and IRAS in the ACT DR5 maps at the 98 GHz, 150 GHz, and 220 GHz frequency bands. In total, we report 167 millimeter counterparts, of which 134 are new identifications. We list the flux density

measurements in the three ACT frequency bands, when available. We analyze the UV-to-millimeter SEDs of 87 galaxies in our sample that fulfill the data requirements. We measure the total IR luminosity from the best-fitting SEDs and investigate the origins of the millimeter emission. The final conclusions of this work can be summarized as the follows:

1. As a result of this work, the number of galaxies detected by ACT has been extended. In particular, the 98 GHz flux densities are new measurements from the recent DR5 maps for the reported IR galaxies in our sample.
2. We report millimeter-wave spectral indices (α_{98-150} , α_{98-220} , and $\alpha_{150-220}$) for our IR galaxy sample, specifying the source type (AGN or DSFG), based on $\alpha_{150-220}$. As expected (since our sample was selected as IR galaxies), the majority of the galaxies in our sample are consistent with the $\alpha_{150-220}$ values of DSFGs. The spectral indices computed from the 98 GHz band α_{98-150} and α_{98-220} are new measurements for ACT-detected galaxies.
3. Using the latest version of CIGALE, V2022.1, we identify the origins of the millimeter emissions using SED fitting. We also show that CIGALE V2022.1 can model SEDs including millimeter bands, with its radio emission decomposition capability. Therefore, we recommend it for studying higher-redshift IR galaxies selected by millimeter radiation.

4. We analyze the SEDs of IR galaxies selected by AKARI and IRAS and detected in the ACT DR 5 maps, for the first time, by including UV, optical, near-IR, mid-IR, FIR, and millimeter data in CIGALE v2022. As a result, we measure important physical parameters of these galaxies, including $L(\text{IR})_{\text{TOTAL}}$, L_{dust} , $L(\text{IR})_{\text{AGN}}$, frac_{AGN} , and ψ_{AGN} . We quantify the relationships between the $L(\text{IR})_{\text{TOTAL}}$ and $L(\text{IR})_{\text{AGN}}$ luminosities and the 98 GHz, 150 GHz, and 220 GHz band luminosities measured from the SED models. These relations can be used as practical tools for inferring the AGN and total IR luminosities from the single millimeter-band luminosities, especially for galaxies with redshift measurements but without multi wavelength UV-to-radio data, to model their SEDs.

5. Our analysis shows that the origins of the millimeter emission can be identified by the decomposition of the radio emission. We find that for more than half of our sample, the origin of the millimeter emission is from AGN and/or SF synchrotron emission, while in only six of 87 galaxies, the millimeter emission is produced by the dust emission. We also provide millimeter color ranges that indicate the different origins of the millimeter emission.

We thank the anonymous reviewer for the insightful and constructive comments. E.K. thanks Oğuzhan Tekin for his technical support. T.G. acknowledges the support from the National Science and Technology Council of Taiwan, through grants 108-2628-M-007-004-MY3 and 110-2112-M-005-013-MY3. T.H. acknowledges support from the National Science and Technology Council of Taiwan, through grants 110-2112-M-005-013-MY3, 110-2112-M-007-034-, and 111-2123-M-001-008-.

This research is based on observations made with AKARI, a JAXA project, with the participation of ESA. This research has made use of the NASA/IPAC Extragalactic Database (NED), which is funded by the National Aeronautics and Space Administration and operated by the California Institute of Technology. Funding for the Sloan Digital Sky Survey IV has been provided by the Alfred P. Sloan Foundation, the U.S. Department of Energy Office of Science, and the Participating Institutions. SDSS-IV acknowledges support and resources from the Center for High Performance Computing at the University of Utah. The SDSS website is www.sdss.org.

SDSS-IV is managed by the Astrophysical Research Consortium for the Participating Institutions of the SDSS Collaboration, including the Brazilian Participation Group, the Carnegie Institution for Science, Carnegie Mellon University, Center for Astrophysics — Harvard & Smithsonian, the Chilean Participation Group, the French Participation Group, Instituto de Astrofísica de Canarias, The Johns Hopkins University, Kavli Institute for the Physics and Mathematics of the Universe (IPMU) / University of Tokyo, the Korean Participation Group, Lawrence Berkeley National Laboratory, Leibniz Institut für Astrophysik Potsdam (AIP), Max-Planck-Institut für Astronomie (MPIA Heidelberg), Max-Planck-Institut für Astrophysik (MPA Garching), Max-Planck-Institut für Extraterrestrische Physik (MPE), National Astronomical Observatories of China, New Mexico State University, New York University, University of Notre Dame, Observatório Nacional / MCTI, The Ohio State University, Pennsylvania State University, Shanghai Astronomical Observatory, United Kingdom Participation Group, Universidad Nacional Autónoma de México, University of Arizona, University of Colorado Boulder, University of Oxford, University of Portsmouth, University of Utah, University of Virginia, University of Washington, University of Wisconsin, Vanderbilt University, and Yale University.

This publication makes use of data products from the Two Micron All Sky Survey, which is a joint project of the University of Massachusetts and the Infrared Processing and Analysis Center/California Institute of Technology, funded by the National Aeronautics and Space Administration and the National Science Foundation.

Facilities: ACT, AKARI, WISE, Herschel, GALEX

Software: CIGALE (Boquien et al. 2019), Source-Extractor (Bertin & Arnouts 1996)

APPENDIX

In the following we explain the adopted optimized apertures for the spatially extended sources using the growth curves.

A. GROWTH CURVES OF SPATIALLY EXTENDED SOURCES

The spatially extended sources are selected as described in Section 2.2.3, and they include isolated sources and one merging system. Panels (a) and (b) of Fig. 12 show examples of the spatially extended sources at 150 GHz: one of the isolated galaxies and one of the merging system. Different aperture sizes are tested for the extended sources, to investigate “growth curves”—i.e., the total flux density within the aperture as a function of the aperture size. Panel (c) of Fig. 12 indicates the growth curves of the sources. To estimate noises with different aperture sizes, the random aperture photometries are conducted with different aperture sizes, following the same manner as described in Section 2.2.2. For the isolated extended sources, we adopt the aperture size at which the total flux densities converge (the solid vertical line in Fig. 12c), unless the S/N is lower than 5. The S/N decreases with increasing aperture size for the isolated extended samples in this work. Therefore, some isolated extended sources show $S/N < 5$ at the converged aperture sizes. In such cases, we use the largest aperture sizes, as long as the S/Ns are higher than 5. The merging system presented in Fig. 12b has a close companion. In this case, We adopt a flexible aperture size to avoid the contaminated flux density from the companion galaxy. Using these optimized aperture sizes for the spatially extended sources, their flux densities are measured, instead of the point-source aperture correction.

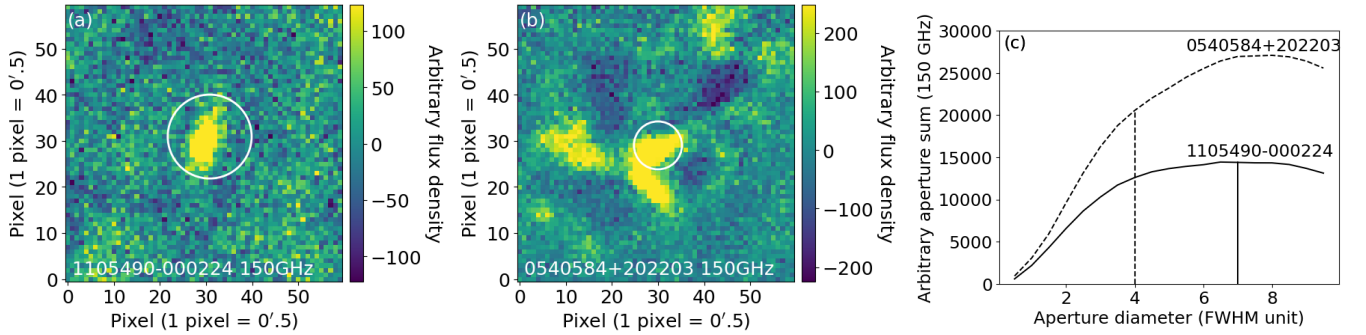


Figure 12. Examples of spatially extended sources at 150 GHz. Left: image of the isolated source matched with AKARI ID 1105490-000224. Middle: image of the merging system matched with AKARI ID 0540584+202203. The white circles indicate the aperture sizes adopted in our analysis. Right: the total flux density within the aperture as a function of the aperture size for sources matched with AKARI IDs 1105490-000224 and 0540584+202203. The solid and dashed lines correspond to 1105490-000224 and 0540584+202203, respectively. The adopted aperture size for 1105490-000224 (0540584+202203) is shown by the solid (dashed) vertical line.

REFERENCES

- Abdurro’uf, Accetta, K., Aerts, C., Silva Aguirre, V., et al. 2022, *ApJS*, 259, 35, doi: [10.3847/1538-4365/ac4414](https://doi.org/10.3847/1538-4365/ac4414)
- AKARI Team. 2020, AKARI/IRC Point Source Catalogue, IPAC, doi: [10.26131/IRSA181](https://doi.org/10.26131/IRSA181)
- Becker, R. H., White, R. L., & Helfand, D. J. 1995, *ApJ*, 450, 559, doi: [10.1086/176166](https://doi.org/10.1086/176166)
- Bertin, E., & Arnouts, S. 1996, *A&AS*, 117, 393, doi: [10.1051/aas:1996164](https://doi.org/10.1051/aas:1996164)
- Böhringer, H., et al. 2004, *A&A*, 425, 367, doi: [10.1051/0004-6361:20034484](https://doi.org/10.1051/0004-6361:20034484)
- Boquien, M., et al. 2019, *A&A*, 622, A103, doi: [10.1051/0004-6361/201834156](https://doi.org/10.1051/0004-6361/201834156)
- Cardelli, J. A., Clayton, G. C., & Mathis, J. S. 1989, *ApJ*, 345, 245, doi: [10.1086/167900](https://doi.org/10.1086/167900)
- Carlstrom, J. E., et al. 2011, *PASP*, 123, 568, doi: [10.1086/659879](https://doi.org/10.1086/659879)

- Casagrande, L., Wolf, C., Mackey, A. D., et al. 2019, *MNRAS*, 482, 2770, doi: [10.1093/mnras/sty2878](https://doi.org/10.1093/mnras/sty2878)
- Casey, C. M., et al. 2021, *ApJ*, 923, 215, doi: [10.3847/1538-4357/ac2eb4](https://doi.org/10.3847/1538-4357/ac2eb4)
- Charlot, S., & Fall, S. M. 2000, *ApJ*, 539, 718, doi: [10.1086/309250](https://doi.org/10.1086/309250)
- Chary, R., & Elbaz, D. 2001, *ApJ*, 556, 562, doi: [10.1086/321609](https://doi.org/10.1086/321609)
- Ciesla, L., et al. 2015, *A&A*, 576, A10, doi: [10.1051/0004-6361/201425252](https://doi.org/10.1051/0004-6361/201425252)
- . 2016, *A&A*, 585, A43, doi: [10.1051/0004-6361/201527107](https://doi.org/10.1051/0004-6361/201527107)
- Clark, C. J. R., et al. 2018, *A&A*, 609, A37, doi: [10.1051/0004-6361/201731419](https://doi.org/10.1051/0004-6361/201731419)
- Clements, D. L., Rowan-Robinson, M., Pearson, C., et al. 2019, *PASJ*, 71, 7, doi: [10.1093/pasj/psy099](https://doi.org/10.1093/pasj/psy099)
- Condon, J. J., et al. 1998, *AJ*, 115, 1693, doi: [10.1086/300337](https://doi.org/10.1086/300337)
- Cutri, R. M., Skrutskie, M. F., van Dyk, S., et al. 2003, *VizieR Online Data Catalog*, II/246
- Cutri, R. M., Wright, E. L., Conrow, T., et al. 2021, *VizieR Online Data Catalog*, II/328
- da Cunha, E., Charlot, S., & Elbaz, D. 2008, *MNRAS*, 388, 1595, doi: [10.1111/j.1365-2966.2008.13535.x](https://doi.org/10.1111/j.1365-2966.2008.13535.x)
- Dale, D. A., & Helou, G. 2002, *ApJ*, 576, 159, doi: [10.1086/341632](https://doi.org/10.1086/341632)
- Dale, D. A., Helou, G., Magdis, G. E., et al. 2014, *ApJ*, 784, 83, doi: [10.1088/0004-637X/784/1/83](https://doi.org/10.1088/0004-637X/784/1/83)
- Das, S., et al. 2011, *ApJ*, 729, 62, doi: [10.1088/0004-637X/729/1/62](https://doi.org/10.1088/0004-637X/729/1/62)
- Datta, R., et al. 2019, *MNRAS*, 486, 5239, doi: [10.1093/mnras/sty2934](https://doi.org/10.1093/mnras/sty2934)
- Delvecchio, I., et al. 2021, *A&A*, 647, A123, doi: [10.1051/0004-6361/202039647](https://doi.org/10.1051/0004-6361/202039647)
- Draine, B. T., et al. 2014, *ApJ*, 780, 172, doi: [10.1088/0004-637X/780/2/172](https://doi.org/10.1088/0004-637X/780/2/172)
- Efstathiou, A., & Rowan-Robinson, M. 2003, *MNRAS*, 343, 322, doi: [10.1046/j.1365-8711.2003.06679.x](https://doi.org/10.1046/j.1365-8711.2003.06679.x)
- Everett, W. B., et al. 2020, *ApJ*, 900, 55, doi: [10.3847/1538-4357/ab9df7](https://doi.org/10.3847/1538-4357/ab9df7)
- Fixsen, D. J. 2009, *ApJ*, 707, 916, doi: [10.1088/0004-637X/707/2/916](https://doi.org/10.1088/0004-637X/707/2/916)
- Fowler, J. W., et al. 2007, *ApOpt*, 46, 3444, doi: [10.1364/AO.46.003444](https://doi.org/10.1364/AO.46.003444)
- Fritz, J., Franceschini, A., & Hatziminaoglou, E. 2006, *MNRAS*, 366, 767, doi: [10.1111/j.1365-2966.2006.09866.x](https://doi.org/10.1111/j.1365-2966.2006.09866.x)
- Goto, T., et al. 2010, *A&A*, 514, A6, doi: [10.1051/0004-6361/200913182](https://doi.org/10.1051/0004-6361/200913182)
- Gralla, M. B., et al. 2020, *ApJ*, 893, 104, doi: [10.3847/1538-4357/ab7915](https://doi.org/10.3847/1538-4357/ab7915)
- Griffin, M. J., et al. 2010, *A&A*, 518, L3, doi: [10.1051/0004-6361/201014519](https://doi.org/10.1051/0004-6361/201014519)
- Hall, N. R., et al. 2010, *ApJ*, 718, 632, doi: [10.1088/0004-637X/718/2/632](https://doi.org/10.1088/0004-637X/718/2/632)
- Helfand, D. J., White, R. L., & Becker, R. H. 2015, *ApJ*, 801, 26, doi: [10.1088/0004-637X/801/1/26](https://doi.org/10.1088/0004-637X/801/1/26)
- Helou, G., Soifer, B. T., & Rowan-Robinson, M. 1985, *ApJL*, 298, L7, doi: [10.1086/184556](https://doi.org/10.1086/184556)
- Helou, G., & Walker, D. W. 1988, *NASA RP-1190*, 7, 0
- Henderson, S. W., et al. 2016, *Journal of Low Temperature Physics*, 184, 772, doi: [10.1007/s10909-016-1575-z](https://doi.org/10.1007/s10909-016-1575-z)
- Hilton, M., et al. 2021, *ApJS*, 253, 3, doi: [10.3847/1538-4365/abd023](https://doi.org/10.3847/1538-4365/abd023)
- Huchra, J., Jarrett, T., Skrutskie, M., et al. 2005, in *Astronomical Society of the Pacific Conference Series*, Vol. 329, *Nearby Large-Scale Structures and the Zone of Avoidance*, ed. A. P. Fairall & P. A. Woudt, 135
- Huchra, J. P., et al. 2012, *ApJS*, 199, 26, doi: [10.1088/0067-0049/199/2/26](https://doi.org/10.1088/0067-0049/199/2/26)
- Ishihara, D., et al. 2010, *A&A*, 514, A1, doi: [10.1051/0004-6361/200913811](https://doi.org/10.1051/0004-6361/200913811)
- Jarrett, T. H., Chester, T., Cutri, R., et al. 2000, *AJ*, 119, 2498, doi: [10.1086/301330](https://doi.org/10.1086/301330)
- Jarvis, M. E., et al. 2020, *MNRAS*, 498, 1560, doi: [10.1093/mnras/staa2196](https://doi.org/10.1093/mnras/staa2196)
- Jones, D. H., Saunders, W., Read, M., & Colless, M. 2005, *PASA*, 22, 277, doi: [10.1071/AS05018](https://doi.org/10.1071/AS05018)
- Jones, D. H., et al. 2004, *MNRAS*, 355, 747, doi: [10.1111/j.1365-2966.2004.08353.x](https://doi.org/10.1111/j.1365-2966.2004.08353.x)
- . 2009, *MNRAS*, 399, 683, doi: [10.1111/j.1365-2966.2009.15338.x](https://doi.org/10.1111/j.1365-2966.2009.15338.x)
- Kelly, B. C. 2007, *ApJ*, 665, 1489, doi: [10.1086/519947](https://doi.org/10.1086/519947)
- Kilerci Eser, E., & Goto, T. 2018, *MNRAS*, 474, 5363, doi: [10.1093/mnras/stx3110](https://doi.org/10.1093/mnras/stx3110)
- Kuźmich, A., Jamroz, M., Bronarska, K., Janda-Boczar, K., & Saikia, D. J. 2018, *ApJS*, 238, 9, doi: [10.3847/1538-4365/aad9ff](https://doi.org/10.3847/1538-4365/aad9ff)
- Le Floch, E., et al. 2005, *ApJ*, 632, 169, doi: [10.1086/432789](https://doi.org/10.1086/432789)
- Lianou, S., Barmby, P., Mosenkov, A. A., Lehnert, M., & Karczewski, O. 2019, *A&A*, 631, A38, doi: [10.1051/0004-6361/201834553](https://doi.org/10.1051/0004-6361/201834553)
- Lonsdale, C. J., Farrah, D., & Smith, H. E. 2006, *Ultraluminous Infrared Galaxies*, ed. J. W. Mason, 285, doi: [10.1007/3-540-30313-8_9](https://doi.org/10.1007/3-540-30313-8_9)
- Malek, K., et al. 2017, *A&A*, 598, A1, doi: [10.1051/0004-6361/201527969](https://doi.org/10.1051/0004-6361/201527969)
- Maraston, C. 2005, *MNRAS*, 362, 799, doi: [10.1111/j.1365-2966.2005.09270.x](https://doi.org/10.1111/j.1365-2966.2005.09270.x)

- Maraston, C., Strömbäck, G., Thomas, D., Wake, D. A., & Nichol, R. C. 2009, *MNRAS*, 394, L107, doi: [10.1111/j.1745-3933.2009.00621.x](https://doi.org/10.1111/j.1745-3933.2009.00621.x)
- Marriage, T. A., et al. 2011, *ApJ*, 731, 100, doi: [10.1088/0004-637X/731/2/100](https://doi.org/10.1088/0004-637X/731/2/100)
- Marsden, D., et al. 2014, *MNRAS*, 439, 1556, doi: [10.1093/mnras/stu001](https://doi.org/10.1093/mnras/stu001)
- Martin, D. C., et al. 2005, *ApJL*, 619, L1, doi: [10.1086/426387](https://doi.org/10.1086/426387)
- Mauch, T., et al. 2003, *MNRAS*, 342, 1117, doi: [10.1046/j.1365-8711.2003.06605.x](https://doi.org/10.1046/j.1365-8711.2003.06605.x)
- Mocanu, L. M., et al. 2013, *ApJ*, 779, 61, doi: [10.1088/0004-637X/779/1/61](https://doi.org/10.1088/0004-637X/779/1/61)
- Murakami, H., et al. 2007, *PASJ*, 59, 369, <https://arxiv.org/abs/0708.1796>
- Murphy, E. J., et al. 2011, *ApJ*, 737, 67, doi: [10.1088/0004-637X/737/2/67](https://doi.org/10.1088/0004-637X/737/2/67)
- . 2012, *ApJ*, 761, 97, doi: [10.1088/0004-637X/761/2/97](https://doi.org/10.1088/0004-637X/761/2/97)
- Murphy, T., et al. 2010, *MNRAS*, 402, 2403, doi: [10.1111/j.1365-2966.2009.15961.x](https://doi.org/10.1111/j.1365-2966.2009.15961.x)
- Naess, S., et al. 2020, *JCAP*, 2020, 046, doi: [10.1088/1475-7516/2020/12/046](https://doi.org/10.1088/1475-7516/2020/12/046)
- Noll, S., Burgarella, D., Giovannoli, E., et al. 2009, *A&A*, 507, 1793, doi: [10.1051/0004-6361/200912497](https://doi.org/10.1051/0004-6361/200912497)
- Onken, C. A., et al. 2019, *PASA*, 36, e033, doi: [10.1017/pasa.2019.27](https://doi.org/10.1017/pasa.2019.27)
- Pilbratt, G. L., et al. 2010, *A&A*, 518, L1, doi: [10.1051/0004-6361/201014759](https://doi.org/10.1051/0004-6361/201014759)
- Planck Collaboration, Ade, P. A. R., Aghanim, N., et al. 2011, *A&A*, 536, A1, doi: [10.1051/0004-6361/201116464](https://doi.org/10.1051/0004-6361/201116464)
- . 2014a, *A&A*, 571, A1, doi: [10.1051/0004-6361/201321529](https://doi.org/10.1051/0004-6361/201321529)
- . 2014b, *A&A*, 571, A15, doi: [10.1051/0004-6361/201321573](https://doi.org/10.1051/0004-6361/201321573)
- . 2016, *A&A*, 594, A26, doi: [10.1051/0004-6361/201526914](https://doi.org/10.1051/0004-6361/201526914)
- Planck Collaboration, Aghanim, N., Akrami, Y., et al. 2020, *A&A*, 641, A1, doi: [10.1051/0004-6361/201833880](https://doi.org/10.1051/0004-6361/201833880)
- Planck Collaboration and Aatrokoski, J. and Ade, P. A. R. and, et al. 2011, *A&A*, 536, A15, doi: [10.1051/0004-6361/201116466](https://doi.org/10.1051/0004-6361/201116466)
- Poglitsch, A., et al. 2010, *A&A*, 518, L2, doi: [10.1051/0004-6361/201014535](https://doi.org/10.1051/0004-6361/201014535)
- Randall, K. E., et al. 2012, *MNRAS*, 421, 1644, doi: [10.1111/j.1365-2966.2012.20422.x](https://doi.org/10.1111/j.1365-2966.2012.20422.x)
- Reuter, C., et al. 2020, *ApJ*, 902, 78, doi: [10.3847/1538-4357/abb599](https://doi.org/10.3847/1538-4357/abb599)
- Rieke, G. H., et al. 2009, *ApJ*, 692, 556, doi: [10.1088/0004-637X/692/1/556](https://doi.org/10.1088/0004-637X/692/1/556)
- Rodighiero, G., et al. 2010, *A&A*, 515, A8, doi: [10.1051/0004-6361/200912058](https://doi.org/10.1051/0004-6361/200912058)
- Rowan-Robinson, M. 2001, *ApJ*, 549, 745, doi: [10.1086/319450](https://doi.org/10.1086/319450)
- Salpeter, E. E. 1955, *ApJ*, 121, 161, doi: [10.1086/145971](https://doi.org/10.1086/145971)
- Sanders, D. B., & Mirabel, I. F. 1996, *ARA&A*, 34, 749, doi: [10.1146/annurev.astro.34.1.749](https://doi.org/10.1146/annurev.astro.34.1.749)
- Saunders, W., et al. 2000, *MNRAS*, 317, 55, doi: [10.1046/j.1365-8711.2000.03528.x](https://doi.org/10.1046/j.1365-8711.2000.03528.x)
- Schlegel, D. J., Finkbeiner, D. P., & Davis, M. 1998, *ApJ*, 500, 525, doi: [10.1086/305772](https://doi.org/10.1086/305772)
- Serra, P., et al. 2011, *ApJ*, 740, 22, doi: [10.1088/0004-637X/740/1/22](https://doi.org/10.1088/0004-637X/740/1/22)
- Skrutskie, M. F., Cutri, R. M., Stiening, R., et al. 2003, 2MASS All-Sky Point Source Catalog, IPAC, doi: [10.26131/IRSA2](https://doi.org/10.26131/IRSA2)
- Spergel, D. N., et al. 2003, *ApJS*, 148, 175, doi: [10.1086/377226](https://doi.org/10.1086/377226)
- Story, K. T., et al. 2013, *ApJ*, 779, 86, doi: [10.1088/0004-637X/779/1/86](https://doi.org/10.1088/0004-637X/779/1/86)
- Su, T., et al. 2017, *MNRAS*, 464, 968, doi: [10.1093/mnras/stw2334](https://doi.org/10.1093/mnras/stw2334)
- Sunyaev, R. A., & Zeldovich, Y. B. 1972, *Comments on Astrophysics and Space Physics*, 4, 173
- Swetz, D. S., et al. 2011, *ApJS*, 194, 41, doi: [10.1088/0067-0049/194/2/41](https://doi.org/10.1088/0067-0049/194/2/41)
- Thornton, R. J., et al. 2016, *ApJS*, 227, 21, doi: [10.3847/1538-4365/227/2/21](https://doi.org/10.3847/1538-4365/227/2/21)
- Toba, Y., et al. 2020, *ApJ*, 899, 35, doi: [10.3847/1538-4357/ab9cb7](https://doi.org/10.3847/1538-4357/ab9cb7)
- Two Micron All Sky Survey Science Team. 2020, 2MASS All-Sky Extended Source Catalog, IPAC, doi: [10.26131/IRSA97](https://doi.org/10.26131/IRSA97)
- Ulrich, M.-H., Maraschi, L., & Urry, C. M. 1997, *ARA&A*, 35, 445, doi: [10.1146/annurev.astro.35.1.445](https://doi.org/10.1146/annurev.astro.35.1.445)
- Urry, C. M., & Padovani, P. 1995, *PASP*, 107, 803, doi: [10.1086/133630](https://doi.org/10.1086/133630)
- van Velzen, S., Falcke, H., Schellart, P., Nierstenhöfer, N., & Kampert, K.-H. 2012, *A&A*, 544, A18, doi: [10.1051/0004-6361/201219389](https://doi.org/10.1051/0004-6361/201219389)
- Vieira, J. D., et al. 2010, *ApJ*, 719, 763, doi: [10.1088/0004-637X/719/1/763](https://doi.org/10.1088/0004-637X/719/1/763)
- Viero, M. P., et al. 2014, *ApJS*, 210, 22, doi: [10.1088/0067-0049/210/2/22](https://doi.org/10.1088/0067-0049/210/2/22)
- Vika, M., Ciesla, L., Charmandaris, V., Xilouris, E. M., & Leboutteiller, V. 2017, *A&A*, 597, A51, doi: [10.1051/0004-6361/201629031](https://doi.org/10.1051/0004-6361/201629031)
- Werner, M. W., et al. 2004, *ApJS*, 154, 1, doi: [10.1086/422992](https://doi.org/10.1086/422992)

- Wolf, C., et al. 2018, PASA, 35, e010,
doi: [10.1017/pasa.2018.5](https://doi.org/10.1017/pasa.2018.5)
- Wright, A. E., Griffith, M. R., Burke, B. F., & Ekers, R. D.
1994, ApJS, 91, 111, doi: [10.1086/191939](https://doi.org/10.1086/191939)
- Wright, E. L., Eisenhardt, P. R. M., Mainzer, A. K., et al.
2010, AJ, 140, 1868, doi: [10.1088/0004-6256/140/6/1868](https://doi.org/10.1088/0004-6256/140/6/1868)
- Wright, Edward L. et al. 2019, AllWISE Source Catalog,
IPAC, doi: [10.26131/IRSA1](https://doi.org/10.26131/IRSA1)
- Yamamura, I., Makiuchi, S., Koga, T., & AKARI Team.
2018, in The Cosmic Wheel and the Legacy of the
AKARI Archive: From Galaxies and Stars to Planets and
Life, ed. T. Ootsubo, I. Yamamura, K. Murata, &
T. Onaka, 227–230
- Yang, G., et al. 2022, ApJ, 927, 192,
doi: [10.3847/1538-4357/ac4971](https://doi.org/10.3847/1538-4357/ac4971)
- York, D. G., et al. 2000, AJ, 120, 1579, doi: [10.1086/301513](https://doi.org/10.1086/301513)
- Zavala, J. A., et al. 2021, ApJ, 909, 165,
doi: [10.3847/1538-4357/abdb27](https://doi.org/10.3847/1538-4357/abdb27)